Research article

JGS
Journal of the Geological Society

Published online September 4, 2019

https://doi.org/10.1144/jgs2018-153 | Vol. 177 | 2020 | pp. 31–49

Two Neoarchean tectonothermal events on the western edge of the North Atlantic Craton, as revealed by SIMS dating of the Saglek Block, Nain Province, Labrador

Daniel J. Dunkley[1,2]*, Monika A. Kusiak[3], Simon A. Wilde[2], Martin J. Whitehouse[4], Anna Sałacińska[3], Ross Kielman[4] & Patrik Konečný[5]

[1] Faculty of Earth Sciences, University of Silesia in Katowice, ul. Będzińska 60, PL-41206 Sosnowiec, Poland
[2] School of Earth and Planetary Sciences, Curtin University, PO Box U1987, Perth, WA 6845, Australia
[3] Polish Academy of Sciences, Institute of Geological Sciences, ul. Twarda 51/55, PL-00818 Warsaw, Poland
[4] Swedish Museum of Natural History, Box 50007, SE-104 05 Stockholm, Sweden
[5] State Geological Institute of Dionýz Štúr, Mlynská dolina 3962/1, 817 04 Bratislava, Slovakia
DJD, 0000-0003-0655-4496; MAK, 0000-0003-2042-8621; SAW, 0000-0002-4546-8278; RK, 0000-0003-0984-3074
* Correspondence: daniel.dunkley@us.edu.pl

Abstract: The Saglek Block forms the northern part of the Nain Province and underwent widespread metamorphism at *c.* 2.7 Ga, producing the dominant gneissosity and intercalation of supracrustal sequences. Zircon dating of gneiss samples collected along 80 km of the Labrador coast from Ramah Bay in the north to Hebron Fjord in the south confirms the widespread extent of high-grade metamorphism between 2750 and 2700 Ma. In addition, a distinct event between 2550 and 2510 Ma produced felsic melt with peritectic garnet in metavolcanic gneiss and granoblastic recrystallization in mafic granulite. Ductile deformation of granite emplaced at *c.* 2550 Ma indicates that this later event involved a degree of tectonism during high-*T* metamorphism. Such tectonism may be related to a hypothesized post-2.7 Ga juxtaposition of the predominantly Eoarchean Saglek Block against the Mesoarchean Hopedale Block, along a north–south boundary that extends from the coast near Nain to offshore of Saglek Bay. Evidence of reworking of *c.* 2.7 Ga gneisses by *c.* 2.5 Ga tectonothermal activity has been found elsewhere on the margins of the North Atlantic Craton, of which the Nain Province represents the western margin. In particular, a recent suggestion that *c.* 2.5 Ga metamorphic ages along the northern margin of the North Atlantic Craton in SW Greenland may record the final assembly of the craton could also apply to the western margin as represented by the rocks of the Nain Province.

Supplementary material: Plots and geochemical data are available at https://doi.org/10.6084/m9.figshare.c.4567934

Received 9 August 2018; **revised** 9 June 2019; **accepted** 2 July 2019

The dating of gneissic complexes is commonly complicated by the effects of multiple tectonothermal events, each of which can produce belts of highly strained, plastically deformed, partially melted and strongly metamorphosed rocks, with previous geological relationships commonly obscured or obliterated. As zones of crustal weakness and/or rheological contrast, such belts are also loci for tectonic reactivation, and it is important to decipher the sequence and extent of metamorphic and tectonic events that produced the gneisses if meaningful correlations are to be attempted for disparate terranes that underwent subsequently separate geological histories. Here we present new data on the timing of high-grade metamorphism and deformation in the Archean Nain Province of the North Atlantic Craton; namely, in the Torngat Mountains region of northern Labrador.

Geological setting

The Nain Province (Fig. 1a) consists of Archean gneisses that extend for 500 km along the Labrador coast, from Makkovik to Nachvak Fjord (Taylor 1971), with a likely extension to the Avayalik Islands near the tip of the eastern Labrador Peninsula (Scott 1995). It forms the western margin of the North Atlantic Craton, conjugate to southwestern Greenland prior to the opening of the Labrador Sea (Bridgwater *et al.* 1973). To the north and west, the Nain Province was reworked at *c.* 1.8 Ga by the north–south-trending Torngat Orogen, which juxtaposed the North Atlantic Craton with Archean continental terranes in the Churchill Province and Paleoproterozoic arc rocks in the Burwell Domain (Van Kranendonk 1996). The Nain Province has been subdivided into the Saglek and Hopedale blocks, north and south respectively of the town of Nain (Fig. 1a). In the vicinity of Saglek Bay, tonalite–trondhjemite–granodiorite (TTG) gneisses of the Saglek Block are the product of multiple episodes of high-*T* metamorphism and ductile deformation that produced a regional dome and basin pattern elongated in a north–south direction, and delineated by interspersed layers and tectonic enclaves composed of supracrustal (metavolcanic and metasedimentary) rocks (Bridgwater *et al.* 1975; Ryan & Martineau 2012). During the Torngat Orogeny, the Nain Province, along with an unconformably overlying sequence of Paleoproterozoic sediments that include the Ramah Group (Fig. 1), was overthrust by strongly reworked basement gneisses of unknown age (Van Kranendonk & Ermanovics 1990; Rivers *et al.* 1996).

A section of the Saglek Block investigated in recent studies by the same group (Kusiak *et al.* 2018; Sałacińska *et al.* 2018, 2019; Whitehouse *et al.* 2019) extends for 80 km along the Labrador coast, from Ramah Bay in the north to Hebron Fjord in the south (Fig. 1b). Gneisses in the southern part of the section formed in several stages throughout the Archean, with the oldest and most abundant TTG-type protoliths (the Uivak gneiss) formed between *c.* 3850 and 3600 Ma (Schiøtte *et al.* 1989; Komiya *et al.* 2017; Kusiak *et al.* 2018; Sałacińska *et al.* 2018, 2019), with lesser episodes of felsic plutonism at *c.* 3.3–3.0, 2.7 and 2.5 Ga (Schiøtte *et al.* 1990, 1992; Krogh & Kamo 2006; Komiya *et al.* 2015; Sałacińska *et al.* 2019). Krogh & Kamo (2006) suggested that TTG

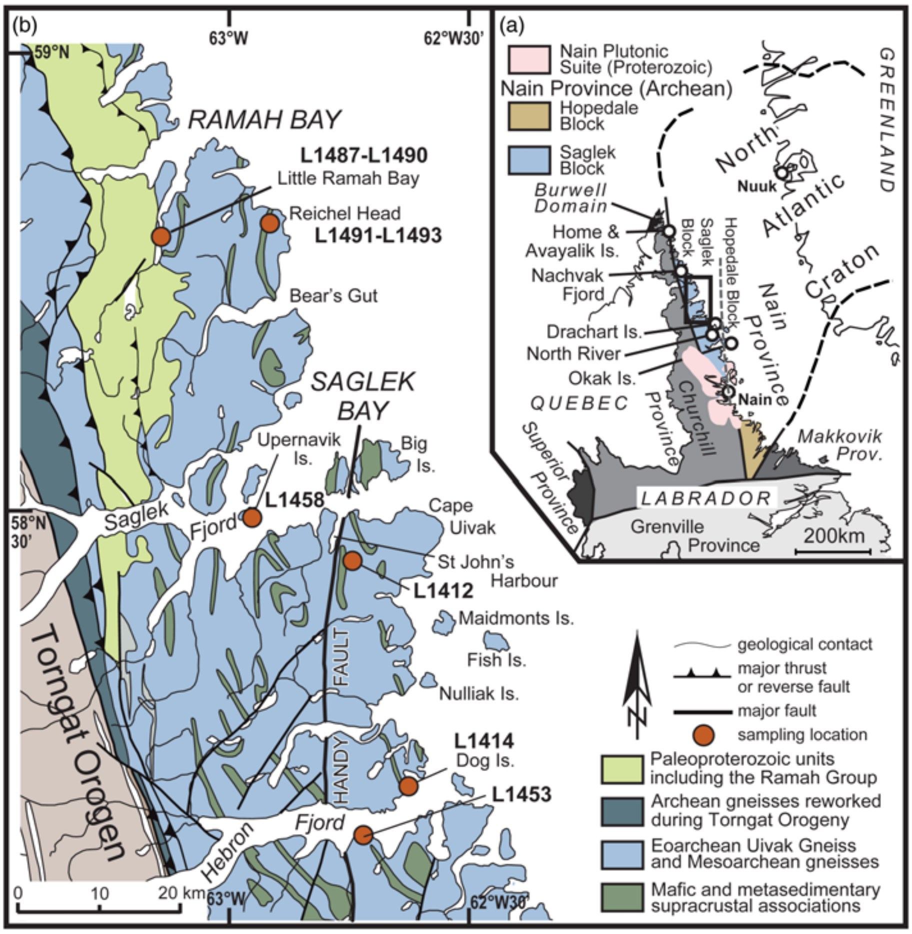

Fig. 1. (**a**) The western part of the North Atlantic Craton (NAC), as defined by the dashed line (after St-Onge *et al.* 2009). The location of study area within the Nain Province is shown. (**b**) Sketch map of part of the Saglek Block investigated in this study.

gneisses from outcrops around Saglek Bay differ in age across the Handy Fault (Fig. 1), with *c.* 3.6 Ga protoliths to the west and *c.* 3.3 Ga to the east. However, recent dating (Komiya *et al.* 2015; Kusiak *et al.* 2018; Sałacińska *et al.* 2018, 2019) revealed complicated and tectonized relationships between Eoarchean and younger TTG gneisses on both sides of the fault. Metamorphosed supracrustal assemblages of sedimentary and volcanic rocks, with associated ultramafic gneisses, occur as discontinuous layers within gneissosity typically less than 100 m thick, and have been divided into sparsely distributed pre- or syn-Uivak supracrustal rocks (the Nulliak assemblage) and post-Uivak Meso- to Neoarchean Upernavik supracrustal rocks (Bridgwater & Schiøtte 1991). Isotopic U–Pb and Hf data from detrital zircon from Upernavik metasediments indicate deposition after *c.* 3.0 Ga, and it has been suggested that this unit includes unrelated supracrustal packages with various ages of deposition (Schiøtte *et al.* 1992). Similarly, there is some uncertainty about the age of deposition of volcanic rocks and sediments that in part formed the Nulliak assemblage. Detrital zircons with an age of *c.* 3850 Ma (Nutman & Collerson 1991) supported deposition after that time, but Komiya *et al.* (2015) and Shimojo *et al.* (2016) favoured a greater antiquity, namely, >3.9 Ga, for these rocks. Whitehouse *et al.* (2019) have recently questioned this, suggesting that there is confusion over the assignment of metasedimentary and mafic gneisses to the Nulliak or Upernavik 'assemblages'. Graphite-bearing metasediments, claimed by Komiya *et al.* (2015) to belong to the Nulliak assemblage, contain detrital zircon that demonstrate a much younger provenance (see Whitehouse *et al.* 2019, after Schiøtte *et al.* 1992). Also, mafic tectonic enclaves near Nulliak Is. that were assigned to the Nulliak assemblage on the map by Ryan & Martineau (2012) have Sm–Nd isotopic signatures that show that some of these are much younger than the enclosing Uivak gneiss (Morino *et al.* 2017). In the absence of more extensive direct dating of tectonic enclaves and belts, the true age of many of the supracrustal rocks in the Saglek Block remains in question.

The assembly of the Saglek Block, comprising the Eoarchean Uivak gneiss, Mesoarchean tonalitic to gabbroic gneisses, and supracrustal packages, may be attributed to *c.* 2.7 Ga tectonism during the widespread high-*T* metamorphism (Schiøtte *et al.* 1990; Krogh & Kamo 2006; Kusiak *et al.* 2018; Sałacińska *et al.* 2018). The above-cited studies were mostly focused around Saglek Bay, but *c.* 2.7 Ga metamorphic zircon was also identified as far south as Drachart Island (Schiøtte *et al.* 1990), and as far north as the Avayalik Islands near the tip of the eastern Labrador pensinsula, where Scott (1995) proposed an extension of the Nain Province as reworked crust within the Torngat Orogen. A corresponding *c.* 2.7 Ga craton-forming event is recognized in similar gneisses on the conjugate section of southwestern Greenland (e.g. Nutman *et al.* 2004, 2013; Kirkland *et al.* 2018).

Post-dating the formation of the gneisses in the Saglek Block, 2.5 Ga mineral ages (U–Pb zircon, monazite and titanite, and K–Ar hornblende; see Discussion for references) have been attributed to the thermal and hydrothermal effects of post-tectonic granitic magmatism (Baadsgaard *et al.* 1979; Schiøtte *et al.* 1992). Alternatively, *c.* 2.5 Ga monazite and titanite ages from offshore drilling samples collected by Wasteneys *et al.* (1996), along with *c.* 2.7 Ga ages of detrital zircon, led Connelly & Ryan (1996) to infer a north–south-trending tectonic boundary between the Saglek and Hopedale blocks. The Hopedale Block comprises late Paleoarchean to Neoarchean protoliths metamorphosed at *c.* 3.0–2.8 Ga. The inferred boundary with the Saglek Block extends offshore north of Nain; but has not been directly observed, being obscured by the extensive Proterozoic Nain Plutonic Suite. Connelly & Ryan (1996) suggested a link between the Saglek–Hopedale boundary and the

Okak shear zone (van Kranendonk & Helmstaedt 1990), to the south. The Okak shear deforms a granitic pluton on Okak Island (Fig. 1), which was inferred by Schiøtte *et al.* (1992) to have an age of *c.* 2.5 Ga (based on unpublished data of Roddick and van Kranendonk and the age of metamorphic monazite in adjacent metasediments).

More recent monazite dating by Kusiak *et al.* (2018) has increased the known extent of high-temperature metamorphism at both *c.* 2.7 and *c.* 2.5 Ga in the Saglek Block between Ramah Bay and Hebron Fjord. However, it is not clear whether these ages represent a prolonged period of high-*T* metamorphism, a gneiss-forming event with subsequent passive thermal activity and granite emplacement, or two discrete tectonothermal events. The purpose of this paper is to re-evaluate the timing and significance of deformation and metamorphism in the Saglek Block, utilizing new U–Pb isotopic dating of zircon and monazite.

Field relationships

This study investigates the sequence of deformation events in the Saglek Block, based on coastal field work between Ramah Bay and Hebron Fjord (Fig. 1), conducted by our team in 2014 and 2017, and the scheme by van Kranendonk & Helmstaedt (1990) for the North River–Nutak area, 100 km south of Saglek Bay. In almost all localities, pre-deformation relationships between the diverse rock types have been transposed into a high-strain gneissosity and a multistage deformational history has long been recognized (Morgan 1975; Collerson & Bridgwater 1979; Schiøtte *et al.* 1990). Because gneissosity affects both Eoarchean and younger Archean TTG protoliths, as well as Mesoarchean Upernavik supracrustal rocks, and because published age data indicate widespread zircon and monazite growth during metamorphism at *c.* 2.7 Ga (Bridgwater & Schiøtte 1991), this may have been the tectonothermal event during which the Saglek Block was assembled. Commonly observed intrafolial folds of gneissic laminations are indications of high-strain ductile deformation (D_1) prior to that which produced the dominant gneissosity (D_2). The dominant gneissosity is in most places vertical to steeply dipping, with lesser domains of low-angle layering, such as that observed on the cliff face at Cape Uivak (Fig. 2a). The difference between D_1 and D_2 structures can be observed where S_2 flattens leucosome in gneisses with S_1 gneissosity and/or mineral foliation (Fig. 2b–d). Elsewhere, S_1 has been transposed into a high-strain, moderately dipping to subvertical gneissic S_2, which trends predominantly north–south. It is unknown whether D_2 significantly postdates D_1, but because it transposes D_1 fabrics in late Mesoarchean to early Neoarchean Upernavik supracrustal rocks, as well as older TTG gneisses, and no intrusive rocks separate D_1 and D_2, it is likely that they represent stages of a single tectonothermal event. Dating of gneisses with Eoarchean protoliths has established an additional, much older episode of high-grade metamorphism at *c.* 3.6 Ga (Sałacińska *et al.* 2018, 2019); however, no large-scale structures have been distinguished in the field that relate to this earlier event. In outcrops *c.* 100 km to the south of Saglek Bay, van Kranendonk & Helmstaedt (1990) described ductile thrusting (F_0) in the Upernavik supracrustal rocks and recumbent folding (F_{n+1}) in both supracrustal rocks and TTG gneisses during high-*T*, high-*P* metamorphism. These are low-angle features, in contrast to the predominantly steep north–south-trending nature of S_2 gneissosity in most of the Saglek area. Although it is possible that these relate to the low-angle macrofold at Cape Uivak, the latter, along with recumbent folds on nearby Big Is., have been attributed either to nappes produced during late Archean, regional, asymmetric folding that generated the present map pattern (Bridgwater *et al.* 1975) or else to a separate recumbent folding event superimposed on the gneiss pattern produced by the aforementioned asymmetric folding (B. Ryan, pers. comm. 2019).

Post-D_2 structures tend to be localized. Upright minor folds are found with axial planes parallel to dominant gneissosity, and are interpreted as recording the waning stages of D_2 tectonism. There are abundant granitoid stocks, sills and dykes that cut the dominant gneissosity. Such granitoids have been classified by previous researchers (Bridgwater & Schiøtte 1991; Schiøtte *et al.* 1992) as ‘post-tectonic’, with metamorphism attributed to late syntectonic magmatism in the waning stages of Neoarchean tectonism. However, in many localities between Saglek Bay and Hebron Fjord, granitoid stocks and dykes are strongly deformed, especially on the islands and in eastern coastal regions. On Dog Is., coarse metagranite that intrudes Uivak gneiss has a steep S_3 foliation that is axial planar to open F_3 folds where granitic melt has pooled in fold noses (Fig. 2e). Intense L_3 defined by stretching of recrystallized fabrics in both pre-D_2 gneisses and post-D_2 granitoids indicates high rates of simple shear during the D_3 event. Dynamic recrystallization of granitoid produced augen gneiss 1 km to the east of St John’s Harbour (Fig. 2f), and the augen show alignment with coarse-grained biotite in quartz and orthoclase. This alignment is parallel to that in the matrix, where quartz, feldspar and biotite have recrystallized into an anastomosing S_3 foliation (Fig. 2g). This is consistent with progressive crystallization of the granitoid during a high-strain ductile event. Mylonite micro-shear zones cut across S_3 foliation. There is an increase in D_3 strain eastwards and southeastwards from Saglek Bay to the coast, with increasing development of F_3 meso-to-macro folding with variably plunging fold axes and intense L_3 stretching and recrystallization parallel to fold axes. Such features are possibly related to D_{n+3} structures described by van Kranendonk & Helmstaedt (1990) further south, which they attributed to a large amphibolite-facies shear zone that runs north–south along the coastal fringe of the Saglek Block south of Saglek Bay to Okak Island, where it deforms syntectonic granitic plutons assumed to have intruded at *c.* 2.5 Ga (Schiøtte *et al.* 1992). However, this shear zone involves retrogression of granulites to amphibolite-facies gneisses, whereas no such shear zone-related retrogression in association with D_3 structures is observed around Saglek Bay or in granulites around Hebron Fjord.

Sample selection and description

Several samples were collected for age determination between Ramah Bay and Hebron Fjord (Fig. 1b). Metamorphic grade at these localities varies from amphibolite to granulite facies (Ryan & Martineau 2012), albeit with varying degrees of later lower-grade overprinting, especially around Ramah Bay. The samples include felsic orthogneisses (L1414, L1488, L1489, L1491 and L1493), intermediate orthogneisses having the chemical characteristics of altered volcanic rocks (L1458 and L1487), mafic granulites (L1453 and L1490) and metapelitic gneiss (L1492). A sample of syn-D_3 granitoid (L1412) was also collected. Classification of orthogneisses is based on whole-rock geochemistry, using the total alkali v. silica diagram (Middlemost 1994) for igneous protoliths with <65 wt% SiO_2, and the ternary normative feldspar classification of Barker (1979; after O’Connor 1965). Plots are provided with geochemical data in the supplementary material. Here, samples are briefly described according to structural relationship and locality (Fig. 1b). Mineral modes and major element geochemistry are presented in Tables 1 and 2, respectively.

Fine- to medium-grained grey felsic orthogneisses matching the description of Uivak I gneiss were collected from Reichel Head (L1491, L1493), Little Ramah Bay (L1488, L1489) and Dog Island (L1414). All have granoblastic fabrics with S_2 defined by millimetre- to centimetre-scale quartzofeldspathic layers (leucosome) and aligned biotite with or without hornblende. Leucosome consisting of intergrown quartz and feldspar (Fig. 3a) or quartz and mesoperthite (Fig. 2d), which is coarser than the granoblastic fabric

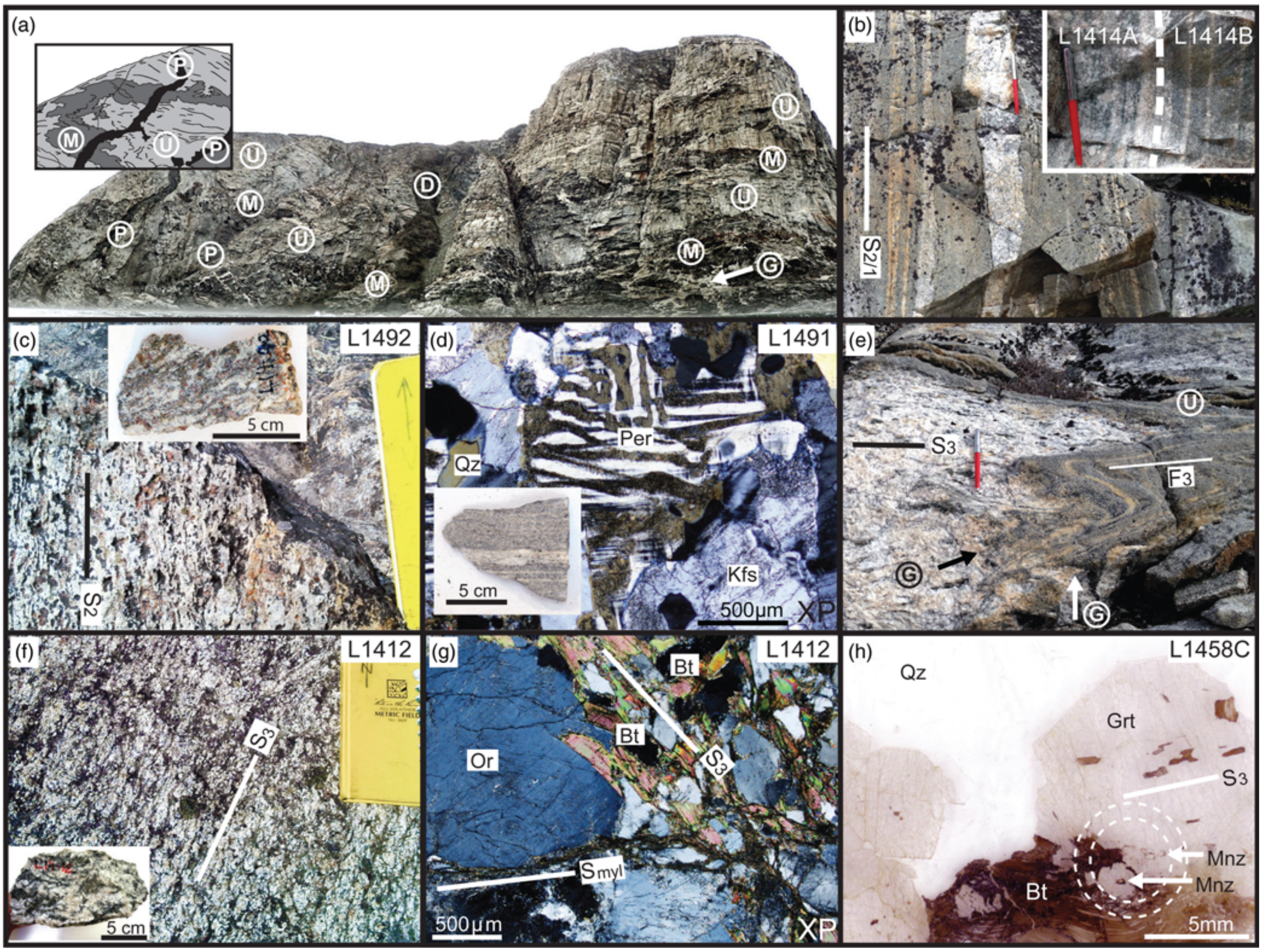

Fig. 2. Macroscopic to microscopic structural relationships in the Saglek Block. (**a**) View of Cape Uivak to SW, showing macroscopic recumbent fold (possibly F_2) defined by a tens of metres thick layer of mafic orthogneiss (M) and disrupted by webby networks of post-D_2 granite (G). Fold nose closes to left as shown in the inset sketch; to the right, the limbs are parallel to dominant S_2 gneissosity in Uivak gneiss (U). Gneisses are intruded by subvertical Proterozoic 'Domes' (D) and Phanerozoic (P) mafic dykes. Width of view (WOV) *c.* 800 m; cliff on right is around 350 m high. (**b**) Intense vertical composite $S_{2/1}$ gneissosity in grey Uivak gneiss on Dog Is., with transposed S_2 granitic laminations. WOV 1 m. Inset: close-up of lower right after sampling, matching division of sample L1414 into part A (coarser metagranitic gneiss with S_2-flattened and recrystallized patches of mafic phases) and part B (grey gneiss with stronger $S_{2/1}$ gneissosity. (**c**) Intense vertical S_2 gneissosity and foliation defined by biotite and sillimanite in metapelitic gneiss, Reichel Head. WOV 30 cm. Inset: sample L1492 of metapelite. (**d**) Crossed polars microphotograph of mesoperthite in S_2-flattened granitic lamination from sample L1491 of grey Uivak gneiss, Reichel Head. WOV 3 mm. Inset: sample L1491, with granitic lamination in trondhjemitic grey gneiss. (**e**) Intrusion of coarse-grained granite (G) across gneissosity in grey Uivak gneiss, prior to or during D_3 folding and formation of axial planar S_3. Dog Is., WOV 1 m. (**f**) Steep north-trending S_3 foliation and recrystallization in metagranite 1 km SE of St John's Harbour. WOV 40 cm. Inset: sample L1412 of metagranite. (**g**) Crossed polars microphotograph of sample L1412, showing margin of magmatic orthoclase including biotite aligned parallel to S_3 foliation defined by biotite in matrix. A mylonite microplane (S_{myl}) cuts S_3 across the lower half of the image. WOV 3 mm. (**h**) Polished thin section from sample L1458C of metavolcanic gneiss, Upernavik Is. Garnet porphyroblast contains inclusions of biotite, monazite and other minerals aligned with strong S_3 foliation in adjacent coarse-grained biotite. Circle shows area drilled for *in situ* monazite dating. Qz, quartz; Kfs, K-feldspar; Per, perthite; Or, orthoclase; Bt, biotite; Grt, garnet; Mnz, monazite.

in the host gneiss, has resulted from crystallization of partial melt, with minor recrystallization on grain margins providing evidence of limited subsequent deformation. Samples L1488 and L1489 are representatives of trondhjemitic orthogneisses from Little Ramah Bay that have, respectively, an abundance and a scarcity of nebulitic leucosome. These two samples were combined for the purpose of dating. The leucosome of sample L1414 felsic orthogneiss from Dog Island (Fig. 2b) is stromatic and the host gneiss varies from a patchily heterogeneous texture, interpreted as the recrystallization of a coarse-grained granitoid (L1414A), to a finer-grained, homogeneous pale grey gneiss with few laminations of leucosome (L1414B). Parts A and B were therefore dated separately.

Mafic samples were collected from S_2 layers hosted by TTG orthogneisses at Little Ramah Bay (L1490) and the south shore of Hebron Fjord (L1453). The latter was tentatively assigned by Ryan & Martineau (2012) to the Nulliak supracrustal assemblage; however, the outcrop also contains aluminous metasediments more typical of the Upernavik supracrustal rocks. Both samples have granoblastic texture with two-pyroxene- and hornblende-bearing assemblages typical of mafic granulite generated from basaltic protoliths (Fig. 3b), but L1453 has a stronger foliation, with stromatic leucosome and associated garnet–biotite-rich selvages. A subvertical NW-trending S_2 gneissosity at the Hebron Fjord locality is crenulated by open to tight F_3 folds with SW-dipping axial planar S_3 defined by aligned biotite and NW-plunging axes. Some patches of garnet-leucosome truncate S_2 but are deformed by D_3 structures, indicating partial melting of mafic orthogneiss during both events.

The S_2 gneissosity and stromatic leucosome found in the orthogneisses is also present in sample L1492 of metapelite from Reichel Head (Fig. 2c). The sample is rich in graphite, similar to

Table 1. *Sample locations and modal mineral assemblages*

Sample	Type	Locality	Latitude (N)	Longitude (W)	Qz	Pl	Afs	Bt	Grt	Cpx	Opx	Hbl	Sil	Spl	Crn	Ox	Act	Chl	Ser	Ep	Zrn	Mnz	Ap	Py
L1412	Meta-monzonite	St John's Harbour	58°26.55′	62°46.02′	•••	•••	•••	••								2°		2°	2°		•			
L1414A	Meta-trondhjemite	Dog Island	58°11.57′	62°36.66′	•••	•••	••	••								Ilm		2°	2°		•		•	
L1414B	Trondhjemitic orthogneiss	Dog Island	58°11.57′	62°36.66′	•••	•••	••	••								Ilm		2°	2°		•		•	
L1453	Mafic granulite	Hebron Fjord, S shore	58°08.32′	62°42.63′	••	•••		••	•••	•••	•••	•••				Mag, Ilm		2°	2°		•		•	
L1458A	Metavolcanic gneiss	Upernavik Island	58°29.19′	62°58.52′	•••	•••	••	•••	•••		•••					Rt		2°	2°		•	•	•	
L1458B	Metavolcanic gneiss	Upernavik Island	58°29.19′	62°58.52′	•••	•••	••	•••	•••		•••					Rt		2°	2°		•	•	•	
L1458C	Metavolcanic gneiss	Upernavik Island	58°29.19′	62°58.52′	•••	•••	••	•••	•••							Rt		2°	2°		•	•	•	
L1487	Andesitic orthogneiss	Little Ramah Bay	58°48.04′	63°10.42′	••	•••	••	•		••	•	••				2°	2°	2°	2°	2°	•	•	•	•
L1488	Trondhjemitic orthogneiss	Little Ramah Bay	58°47.99′	63°10.59′	•••	•••	••	••								Ilm		2°	2°	2°	•		•	
L1489	Trondhjemitic orthogneiss	Little Ramah Bay	58°47.75′	63°10.49′	•••	•••	••	•		••						Ilm		2°	2°	2°	•		•	
L1490	Mafic granulite	Little Ramah Bay	58°47.99′	63°10.59′	••	•••		•		•••	•••	•••				Mag, Ilm	2°	2°	2°	2°	•		•	•
L1491	Trondhjemitic orthogneiss	Reichel Head	58°48.90′	62°56.13′	•••	•••	••	••	•							2°		2°	2°	2°	•	•	•	
L1492	Metapelitic gneiss	Reichel Head	58°48.91′	62°56.07′	•••	•••	•••	•••	•••				••	•	•	Spl, Mag, Ilm		2°	2°		•	•	•	•
L1493	Granitic orthogneiss	Reichel Head	58°48.91′	62°56.03′	•••	•••	•••	••	•							2°		2°	2°	2°	•		•	

Latitude and longitude are in degrees and decimal minutes (WGS84 geoid). Major (•••), minor (••) and accessory (•) amounts; 2°, secondary mineral phase. Qz, quartz; Pl, plagioclase; Afs, alkali feldspar; Grt, garnet; Cpx, clinopyroxene; Opx, orthopyroxene; Hbl, hornblende; Bt, biotite; Act, actinolite; Chl, chlorite; Ser, sericite; Ep, epidote; Ox, Fe–Ti oxides; Rt, rutile; Mag, magnetite; Ilm, ilmenite; Spl, spinel; Zrn, zircon; Mnz, monazite; Ap, apatite; Py, pyrite; Crn, corundum; Sil, sillimanite.

metasedimentary rocks that have been claimed to be early Eoarchean in age by Tashiro *et al.* (2017). Garnet poikiloblasts enclose S_2-aligned flakes of biotite, graphite and sillimanite (Fig. 3c). Leucosome rich in K-feldspar and quartz is also flattened into S_2, and the mineral assemblage is characteristic of granulite-facies metamorphism.

Pyroxene–quartz-bearing samples were taken from Little Ramah Bay (L1487) and Upernavik Island (L1458). The former has been described by Kusiak *et al.* (2018), whereas the latter is a typical orthopyroxene–garnet gneiss (Fig. 3d) found interlayered with aluminous and mafic gneisses that form the Upernavik 'assemblage' (Ryan & Martineau 2012). It is more aluminous than typical andesite, but unlike metapelite from the same locality, it contains abundant orthopyroxene, and is chemically characteristic of altered metavolcanic or volcanoclastic rocks, similar to Mesoarchean deposits at Qussuk and Storø in southwestern Greenland (Szilas *et al.* 2016, 2017). Composition grades across S_2 gneissic layers from orthopyroxene–plagioclase (L1458A) to garnet–biotite (L1458B) gneiss; however, the difference is in modal proportion only, and all phases are present in both rock types. Abundant leucosome is present in L1458, as S_2-cutting layers with biotite-rich selvages and euhedral garnet poikiloblasts, as are commonly formed through incongruent melting of pelitic rocks (L1458C; Fig. 3d). Garnet is anhedral and slightly poikilitic in both types, with large inclusions of rutile and quartz (Fig. 3e). The leucosome is quartz-rich and moderately deformed, with warped and recrystallized quartz grains wrapping garnet poikiloblasts that contain S_3-aligned grains of biotite and monazite (Fig. 2h). The presence of coarse biotite flakes aligned with the foliation in biotite-rich selvages, and with the sub-mylonitic recrystallization of quartz in the leucosome, supports the interpretation that garnet formed through incongruent melting of the host gneiss, and that the melt crystallized under stress.

Methods

Detailed analytical protocols and data reduction procedures are provided in the Appendix. Determination of bulk-rock geochemistry for major elements was undertaken by Acme Labs in Vancouver, Canada, through Bureau Veritas, Poland. For Zr-in-rutile thermometry, electron microprobe (EMP) analysis was carried out on a Cameca SX-100 instrument at the Electron Microprobe Laboratory, State Geological Institute of Dionýza Štúra, Bratislava, Slovakia. For ion microprobe analysis, plugs drilled from polished thin sections, and monazite and zircon mineral grains separated from crushed samples, were mounted in epoxy, polished and imaged by scanning electron microscope (SEM) with backscattered electron (BSE) and cathodoluminescence (CL) detectors at the John de Laeter Centre, Curtin University, Western Australia. Isotopic U–Pb dating of zircon and monazite grains was by sensitive high-resolution ion microprobe (SHRIMP II) at the John de Laeter Centre, Curtin University in Perth, Western Australia, and by CAMECA IMS 1280 ion microprobe at the NordSIMS facility, Swedish Museum of Natural History, Stockholm. All ion microprobe data are quoted with 1σ analytical errors, whereas weighted mean and discordia intercept ages are quoted at 95% confidence levels, and include the decay-constant error of the concordia curve.

Results

Rutile thermometry

The abundance of rutile in sample L1458 allowed for *in situ* EMP analysis of zirconium contents to estimate temperatures of mineral growth. The formulation of Watson *et al.* (2006) was used; data are

Table 2. *Whole-rock major oxide (wt%) and normative compositions*

Sample:	L1412	L1414A	L1414B	L1458B	L1487	L1488	L1489	L1490	L1491	L1492	L1493
SiO_2	58.88	69.10	66.80	60.88	54.94	70.90	66.70	44.90	69.57	57.10	74.70
TiO_2	0.52	0.14	0.29	0.75	0.89	0.26	0.45	3.13	0.26	0.73	0.05
Al_2O_3	20.24	17.40	18.00	11.94	16.91	15.90	17.70	11.30	16.64	19.80	14.40
ΣFe_2O_3	4.80	1.48	2.15	12.79	7.44	1.50	2.61	22.20	1.97	5.01	0.63
MnO	0.06	n.d.	n.d.	0.24	0.09	n.d.	n.d.	0.31	n.d.	n.d.	n.d.
MgO	2.16	0.90	1.29	9.85	4.54	0.86	1.40	4.64	0.55	2.40	0.12
CaO	3.73	2.34	2.30	1.23	6.23	2.07	1.98	9.04	2.56	1.17	1.34
Na_2O	5.84	6.20	6.34	1.74	3.63	5.47	5.52	1.79	5.69	0.75	4.70
K_2O	2.50	1.43	1.94	0.25	1.49	2.19	2.30	0.93	1.66	11.10	3.62
P_2O_5	0.12	n.d.	0.13	n.d.	0.36	0.08	0.12	0.30	0.06	0.12	n.d.
SO_2	n.d.	n.d.	0.05	n.d.	0.26	n.d.	n.d.	0.29	n.d.	n.d.	n.d.
LOI	1.00	0.84	0.89	0.00	3.10	0.88	1.48	0.66	0.90	1.71	0.22
Sum	99.85	99.83	100.18	99.67	99.88	100.11	100.26	99.49	99.86	99.89	99.78
Qz	2.0	20.6	15.0	25.5	6.2	24.5	18.6	–	23.0	2.1	30.2
Crn	1.4	1.5	1.6	6.6	–	1.0	2.8	–	1.0	4.7	0.3
Or	14.8	8.5	11.5	1.5	8.8	12.9	13.6	5.5	9.8	65.6	21.4
Ab	49.4	52.5	53.6	14.7	30.7	46.3	46.7	15.1	48.1	6.3	39.8
An	17.7	11.3	10.6	6.0	25.4	9.7	9.0	20.1	12.3	5.0	6.6
Di	–	–	–	–	2.5	–	–	19.3	–	–	–
Hy	10.8	3.9	5.5	40.1	17.8	3.7	6.1	24.4	3.5	11.2	1.0
Ol	–	–	–	–	–	–	–	0.5	–	–	–
Mag	1.0	0.3	0.5	2.8	1.6	0.3	0.6	4.8	0.4	1.1	0.1
Ilm	1.0	0.3	0.6	1.4	1.7	0.5	0.9	5.9	0.5	1.4	0.1
Ap	0.3	0.1	0.3	–	0.9	0.2	0.3	0.7	0.1	0.3	–
Py	–	–	0.1	–	0.5	–	–	0.5	–	–	–

Qz, quartz; Crn, corundum; Or, orthoclase; Ab, albite; An, anorthite; Di, diopside; Hy, hypersthene; Ol, olivine; Mag, magnetite; Ilm, ilmenite; Ap, apatite; Py, pyrite. Total Fe oxide shown as Fe_2O_3. $Fe_2O_3/FeO = 0.15$ assumed for normative calculations. LOI, loss on ignition.

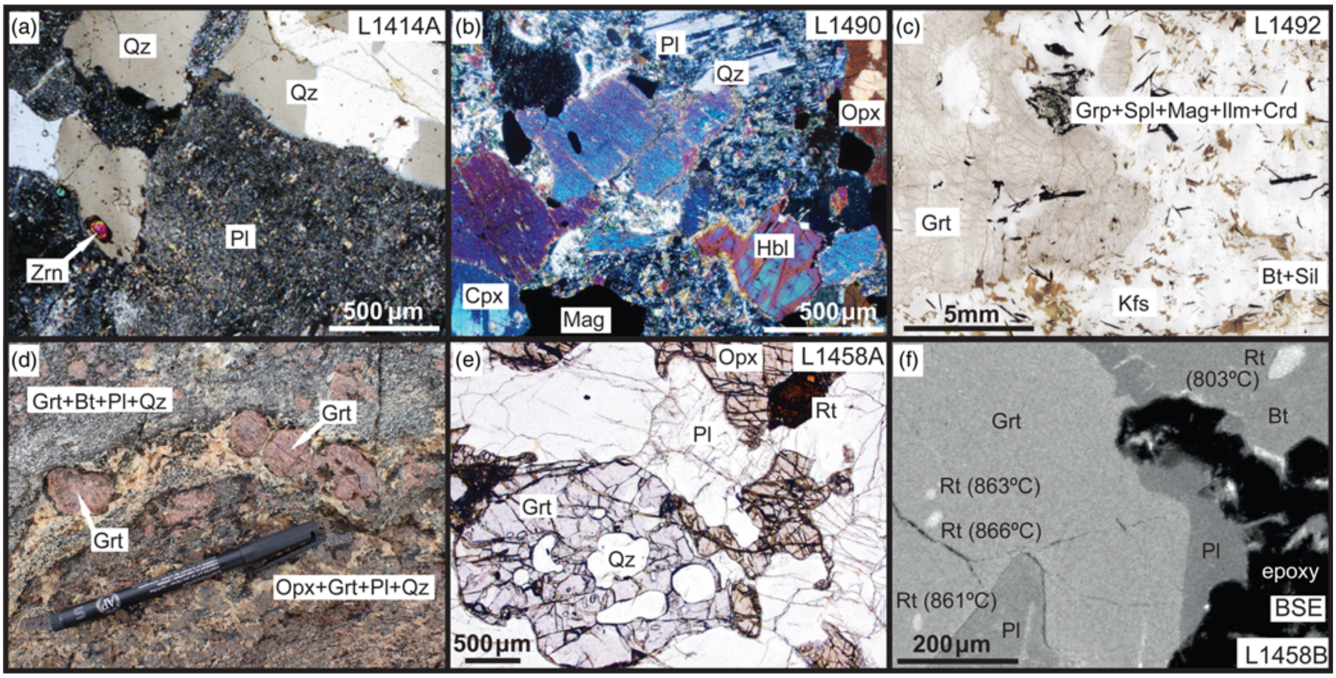

Fig. 3. Mineral relationships in gneisses of the Saglek Block. All are photomicrographs except (**d**). (**a**) Weak S_2 fabric in coarsely recrystallised metagranitic lamination from sample L1414A, Dog Is. Prismatic zircon crystal is aligned parallel to S_2. Plagioclase has been strongly sericitized. Crossed polars, WOV 4 mm. (**b**) Granoblastic texture in sample L1490, mafic granulite from Little Ramah Bay, with extensive alteration of mafic minerals and sericitization of plagioclase. Crossed polars, WOV 4 mm. (**c**) Porphyroblastic texture in sample L1492 of metapelite from Reichel Head. Dark clot is an intergrowth of graphite, spinel, magnetite, ilmenite and cordierite. Transmitted light, WOV 2 cm. (**d**) Outcrop photograph of metavolcanic gneiss, showing rock types (A, B and C) found in sample L1458 from Upernavik Is. Type A is granoblastic orthopyroxene- and garnet-bearing gneiss (bottom); type B is garnet- and biotite-rich gneiss (top); type C is felsic neosome with idioblastic garnet (middle). Biotite selvages around garnet idioblasts and on the margins of the neosome, formed by back-reaction during crystallization of felsic melt, should be noted. WOV 15 cm. (**e**) Xenoblastic garnet in sample L1458A, in granoblastic gneiss with rutile, plagioclase and orthopyroxene; the latter occurs as both xenoblasts and discontinuous rims between garnet and plagioclase. Transmitted light, WOV 4 mm. (**f**) BSE image of sample L1458B, showing rutile inclusions in garnet and biotite. Zirconium-in-rutile temperature estimates obtained by electron microprobe. Qz, quartz; Zrn, zircon; Pl, plagioclase; Opx, orthopyroxene; Cpx, clinopyroxene; Hbl, hornblende; Mag, magnetite; Kfs, K-feldspar; Grt, garnet; Bt, biotite; Sil, sillimanite; Grp, graphite; Spl, spinel; Ilm, ilmenite; Crd, cordierite; Rt, rutile.

Table 3. *EMP analyses of Zr in rutile, sample L1458B*

Analysis	Location	% ZrO_2	Total	% atomic Zr	±2σ	*T* (°C)	±2σ
d1/1	In plagioclase	0.2450	100.10	0.1815	0.0045	816.8	5.7
d2/1	In plagioclase	0.1277	100.04	0.0946	0.0038	746.5	8.0
d3/1	In plagioclase	0.1511	102.78	0.1119	0.0039	761.0	7.2
d4/1	In plagioclase	0.1515	101.64	0.1122	0.0039	762.4	7.2
d7/1	In garnet	0.3394	94.50	0.2514	0.0051	862.9	5.0
d8/1	In garnet	0.3433	97.45	0.2543	0.0052	860.5	4.0
n3/1	In garnet	0.3622	98.42	0.2683	0.0052	866.0	4.8
n1/1	In biotite	0.2197	101.57	0.1627	0.0043	802.7	5.9

Errors estimated from counting statistics.

provided in Table 3. Three grains of rutile included in garnet from the garnet–biotite-rich part of the sample (L1458B, Fig. 3f) yielded ZrO_2 contents of 0.3394–0.3622 wt%, equivalent to 861–866°C, whereas grains enclosed in plagioclase or biotite yielded more variable, lower contents (0.1277–0.2450 wt%) equivalent to 747–817°C. The former temperatures are the best estimate for the temperature of garnet growth during metamorphism on Upernavik Is., and the estimate is consistent with granulite-facies metamorphism in the Saglek Bay area, as has been suggested by various researchers (e.g. Krogh & Kamo 2006; Ryan & Martineau 2012).

Zircon dating

Zircon grains from all samples are subhedral to anhedral, with cathodoluminescence imaging (Fig. 4) revealing rims with anhedral, graduated or sector zoning typical of growth under

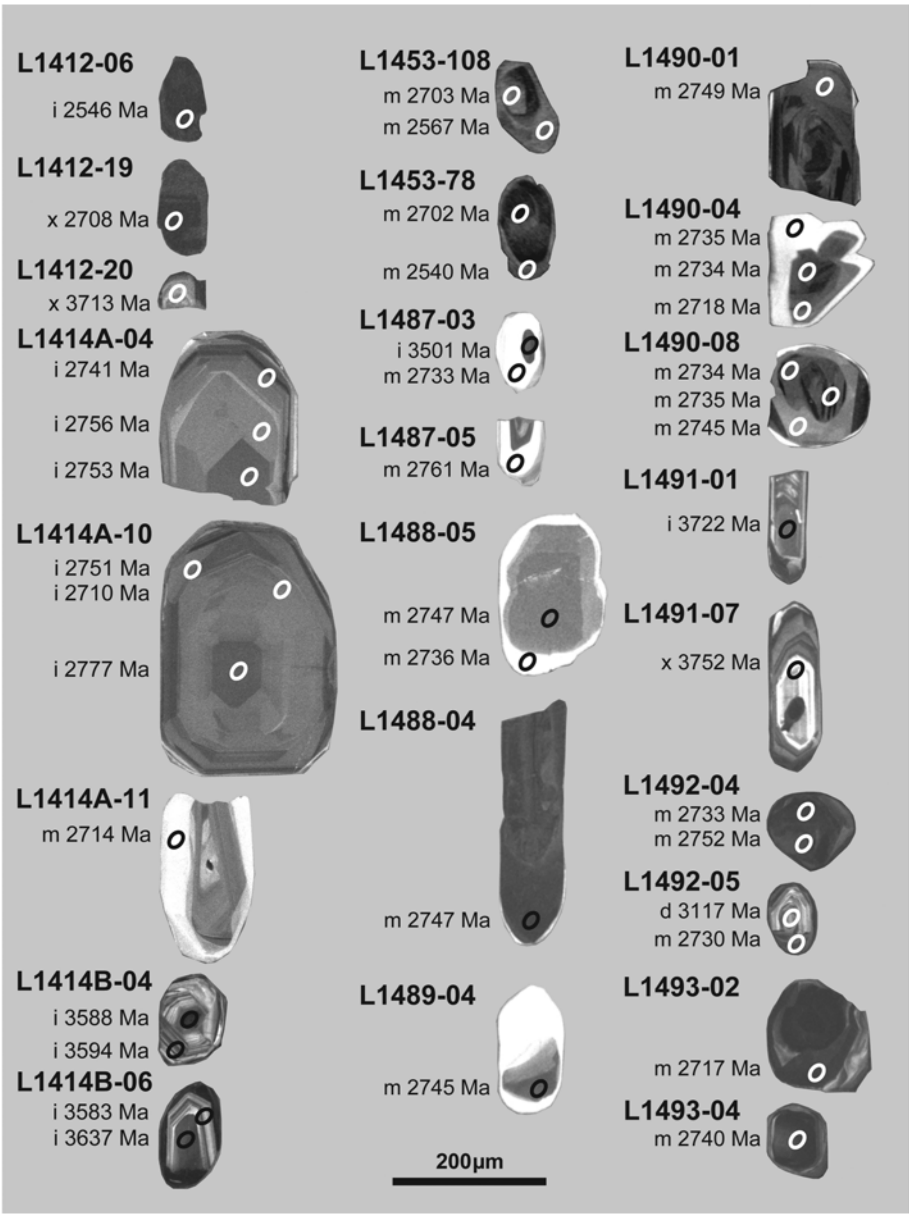

Fig. 4. Cathodoluminescence images of zircon dated by SIMS. Labels show sample and grain numbers; analytical spots labelled with type of zircon (m, metamorphic; i, igneous; x, xenocrystic; d, detrital) and $^{207}Pb/^{206}Pb$ age.

Table 4. *Zircon SIMS U–Th–Pb data*

Sample[1] spot no.	U (ppm)	Th (ppm)	Th/U[2]	Pb (ppm)	$^{206}Pb_c$[3] %	Ratios[4] $^{238}U/^{206}Pb$	±σ (%)	$^{207}Pb/^{206}Pb$	±σ (%)	Ages[4] $^{206}Pb/^{238}U$	±σ	$^{207}Pb/^{206}Pb$	±σ	Disc. %
St Johns Harbour, sample L1412, n5696														
Xenocrystic core														
20.1	83	53	0.59	95.8	0.32	1.298	1.5	0.35148	0.52	3683	41	3713.4	7.8	1
19.1	1030	195	0.18	666.7	0.06	1.909	1.0	0.18609	0.18	2715	22	2707.9	3.0	0
23.1	939	88	0.09	602.6	0.08	1.884	1.0	0.18576	0.20	2744	22	2705.0	3.3	−2
Igneous														
05.1	1033	304	0.29	635.2	0.06	2.030	1.0	0.16938	0.18	2582	21	2551.5	3.0	−1
07.1	502	249	0.48	319.4	0.13	2.043	1.0	0.16932	0.30	2568	22	2550.9	5.0	−1
02.1	707	531	0.73	477.7	0.12	2.021	1.0	0.16916	0.31	2591	22	2549.3	5.2	−2
22.1	681	258	0.37	429.5	0.12	2.011	1.0	0.16915	0.24	2603	22	2549.2	3.9	−3
25.1	1036	267	0.25	638.7	0.07	2.006	1.0	0.16904	0.18	2607	22	2548.1	3.1	−3
06.1	781	403	0.49	498.6	0.08	2.042	1.0	0.16885	0.22	2570	21	2546.3	3.7	−1
27.1	674	265	0.38	420.8	0.08	2.036	1.0	0.16862	0.23	2576	22	2544.0	3.8	−2
12.1	289	77	0.26	175.8	0.13	2.034	1.1	0.16852	0.34	2578	22	2543.0	5.7	−2
26.1	501	216	0.42	313.9	0.11	2.047	1.0	0.16796	0.27	2565	22	2537.4	4.5	−1
Dog Island, sample L1414A, n5546														
Igneous														
12.3	137	68	0.50	96.6	–	1.878	1.3	0.19171	0.44	2752	30	2756.9	7.1	0
04.2	113	75	0.66	83.2	–	1.871	1.5	0.19165	0.45	2760	33	2756.3	7.4	0
12.2	107	32	0.31	73.6	–	1.847	1.5	0.19153	0.42	2789	34	2755.3	6.8	−1
02.1	138	76	0.58	100.4	–	1.849	1.3	0.19153	0.52	2786	30	2755.3	8.5	−1
03.1	170	159	0.96	132.4	–	1.864	1.5	0.19140	0.32	2769	34	2754.3	5.3	−1
09.2	119	80	0.66	87.0	–	1.882	1.2	0.19124	0.47	2747	26	2752.9	7.7	0
04.1	195	168	0.88	149.6	–	1.864	1.5	0.19122	0.31	2769	34	2752.7	5.1	−1
01.3	130	73	0.58	93.9	–	1.877	1.5	0.19102	0.33	2753	33	2751.0	5.4	0
10.2	239	75	0.31	163.6	–	1.866	1.3	0.19100	0.34	2766	30	2750.8	5.6	−1
05.1	166	156	0.91	127.0	–	1.886	1.3	0.19063	0.37	2743	30	2747.6	6.1	0
06.2	153	65	0.42	106.9	0.11	1.862	1.4	0.19056	0.41	2771	32	2747.0	6.7	−1
01.1	76	32	0.45	52.9	–	1.878	1.6	0.19050	0.62	2752	35	2746	10	0
08.2	144	58	0.39	98.7	–	1.889	1.2	0.19036	0.46	2739	26	2745.3	7.6	0
04.2	322	61	0.17	210.0	0.01	1.894	1.6	0.18988	0.34	2733	36	2741.2	5.6	0
08.2	265	111	0.42	185.3	0.03	1.868	1.4	0.18969	0.47	2764	31	2739.5	7.7	−1
01.2	113	53	0.49	80.8	–	1.849	1.7	0.18967	0.67	2787	39	2739	11	−2
03.2	135	59	0.45	94.5	0.04	1.878	1.8	0.18909	0.36	2752	40	2734.2	5.8	−1
Excluded														
10.1	192	158	0.79	146.2	–	1.857	1.7	0.19407	0.39	2777	38	2777.0	6.3	0
12.4	125	72	0.60	93.2	–	1.822	1.6	0.19353	0.39	2820	36	2772.4	6.5	−2
11.2	34	77	2.39	32.8	–	1.892	1.8	0.18679	0.97	2735	40	2714	16	−1
10.3	134	55	0.42	91.4	–	1.906	1.4	0.18628	0.47	2719	30	2709.6	7.7	0
Discordant														
07.1	918	30	0.03	608.7	0.43	1.849	1.5	0.2173	1.7	2787	33	2961	27	7
Dog Island, sample L1414B, n5541														
Igneous and/or xenocrystic														
03.2	53	26	0.49	57.2	0.56	1.363	1.8	0.33968	0.44	3548	48	3661.3	6.8	4
05.1	162	99	0.66	191.8	0.02	1.271	1.4	0.33943	0.26	3741	39	3660.2	3.9	−3
05.3	75	61	0.82	87.7	0.38	1.324	1.5	0.33677	0.47	3626	41	3648.2	7.2	1
05.2	82	50	0.64	93.4	0.25	1.314	1.6	0.33649	0.53	3647	45	3646.9	8.1	0
01.1	158	56	0.36	170.6	0.02	1.322	1.6	0.33546	0.49	3631	46	3642.2	7.5	0
06.1	220	79	0.39	243.6	0.47	1.297	1.4	0.33440	0.35	3685	39	3637.4	5.4	−2
04.2	201	67	0.35	214.8	0.02	1.326	1.3	0.32502	0.26	3622	37	3593.8	3.9	−1
04.1	1131	1526	1.40	1389.5	0.97	1.384	1.3	0.32373	0.36	3506	35	3587.7	5.5	3
06.2	137	49	0.36	143.4	0.04	1.356	1.6	0.32274	0.34	3561	44	3582.9	5.2	1
07.1	341	189	0.54	366.6	0.81	1.364	1.8	0.32159	0.21	3546	50	3577.5	3.3	1
Discordant														
01.2	1991	783	0.27	1160.1	0.66	2.270	1.7	0.2240	2.2	2353	33	3009	35	26
Hebron Fjord, South shore, sample L1453, n5736														
Group 1 metamorphic (excluded from minimum pooled age)														
54.1	70	14	0.183	49.4	0.11	1.788	1.2	0.20276	0.60	2864	28	2848.6	9.7	−1
8.1	106	27	0.274	72.3	0.07	1.842	1.2	0.18967	0.46	2796	27	2739.3	7.6	−3
30.1	181	55	0.308	124.5	0.06	1.852	1.1	0.18917	0.38	2783	25	2735.0	6.2	−2
25.1	100	19	0.195	67.0	–	1.860	1.2	0.18871	0.50	2773	28	2730.9	8.2	−2

(continued)

Table 4. *(Continued)*

Sample[1] spot no.	U (ppm)	Th (ppm)	Th/U[2]	Pb (ppm)	$^{206}Pb_c$[3] %	Ratios[4] $^{238}U/^{206}Pb$	±σ (%)	$^{207}Pb/^{206}Pb$	±σ (%)	Ages[4] $^{206}Pb/^{238}U$	±σ	$^{207}Pb/^{206}Pb$	±σ	Disc. %
34.1	97	26	0.274	65.3	0.07	1.876	1.2	0.18821	0.59	2755	26	2726.6	9.7	−1
64.1	101	20	0.203	65.8	–	1.911	1.4	0.18690	0.44	2713	31	2715.1	7.3	0
37.2	119	29	0.247	78.5	–	1.901	1.1	0.18689	0.47	2725	25	2715.0	7.8	−1
26.1	100	23	0.214	62.5	0.31	1.990	1.2	0.18657	0.56	2624	26	2712.1	9.2	4
Group 1 metamorphic (used for pooled minimum age)														
15.1	308	113	0.365	208.3	0.05	1.904	1.0	0.18633	0.31	2721	23	2710.1	5.1	−1
45.2	133	36	0.263	87.5	0.06	1.905	1.1	0.18633	0.64	2720	25	2710	10	0
57.1	747	169	0.225	483.4	0.03	1.930	1.1	0.18633	0.18	2691	25	2710.1	2.9	1
19.1	542	247	0.455	370.1	0.05	1.919	1.0	0.18620	0.23	2703	23	2708.9	3.8	0
4.2	291	97	0.348	197.5	0.03	1.885	1.0	0.18618	0.34	2743	23	2708.7	5.6	−2
74.1	535	211	0.399	362.8	0.03	1.911	1.3	0.18618	0.25	2714	28	2708.7	4.1	0
4.1	107	25	0.241	70.5	0.05	1.897	1.1	0.18615	0.46	2729	25	2708.4	7.6	−1
41.1	491	170	0.348	331.0	0.05	1.899	1.0	0.18612	0.24	2728	23	2708.2	3.9	−1
69.2	384	133	0.361	260.3	0.03	1.895	1.2	0.18601	0.23	2731	28	2707.2	3.8	−1
21.1	522	219	0.423	356.3	0.02	1.906	1.0	0.18596	0.22	2719	23	2706.8	3.7	−1
41.2	328	109	0.331	220.8	0.08	1.893	1.0	0.18592	0.29	2734	23	2706.4	4.8	−1
45.1	578	152	0.255	381.0	0.06	1.905	1.0	0.18589	0.26	2720	23	2706.1	4.3	−1
3.1	119	27	0.232	77.8	0.06	1.914	1.1	0.18585	0.46	2710	25	2705.8	7.6	0
61.1	563	167	0.286	368.2	0.14	1.935	1.0	0.18578	0.23	2685	23	2705.1	3.7	1
157.2	117	23	0.197	76.9	0.04	1.888	1.4	0.18575	0.45	2740	31	2704.9	7.4	−2
01.1	326	127	0.392	219.5	0.14	1.921	1.0	0.18573	0.27	2702	23	2704.7	4.4	0
54.2	317	104	0.319	212.6	0.10	1.900	1.1	0.18571	0.42	2726	24	2704.5	6.9	−1
85.2	118	30	0.260	77.1	0.08	1.924	1.3	0.18564	0.42	2698	29	2703.9	6.9	0
108.1	46	7	0.155	29.3	–	1.934	1.4	0.18553	0.81	2686	32	2703	13	1
34.2	325	141	0.449	226.4	0.31	1.872	1.1	0.18551	0.46	2759	24	2702.8	7.6	−3
78.1	816	170	0.223	534.1	0.01	1.904	1.3	0.18540	0.28	2721	28	2701.8	4.6	−1
20.1	478	186	0.385	318.7	0.04	1.937	1.0	0.18539	0.24	2683	22	2701.7	3.9	1
25.2	362	98	0.266	235.9	0.19	1.929	1.1	0.18531	0.29	2692	23	2701.0	4.8	0
52.1	86	20	0.223	55.6	0.07	1.924	1.2	0.18528	0.75	2698	26	2701	12	0
5.1	570	148	0.262	376.2	0.03	1.906	1.0	0.18528	0.31	2719	23	2700.7	5.1	−1
12.1	900	297	0.337	607.2	0.11	1.893	1.0	0.18520	0.17	2734	23	2700.0	2.8	−2
157.1	164	51	0.308	106.7	0.02	1.955	1.3	0.18512	0.39	2663	28	2699.3	6.5	2
59.1	239	84	0.355	160.9	0.05	1.906	1.1	0.18506	0.42	2719	24	2698.8	6.9	−1
37.1	959	253	0.257	627.5	0.02	1.919	1.0	0.18501	0.17	2704	22	2698.3	2.8	0
22.2	469	205	0.430	316.7	0.05	1.931	1.0	0.18501	0.24	2690	23	2698.3	3.9	0
58.1	109	34	0.306	72.0	0.03	1.920	1.1	0.18492	0.47	2703	25	2697.5	7.7	0
16.1	269	88	0.325	177.3	0.04	1.935	1.1	0.18491	0.31	2685	24	2697.4	5.0	1
101.2	172	52	0.311	114.0	0.06	1.918	1.3	0.18487	0.41	2704	29	2697.1	6.7	0
49.1	130	45	0.331	87.5	0.06	1.899	1.1	0.18473	0.48	2726	25	2695.8	7.9	−1
23.1	98	21	0.207	65.0	0.16	1.869	1.2	0.18472	0.77	2763	26	2696	13	−3
29.1	192	109	0.580	135.8	0.03	1.895	1.1	0.18470	0.55	2732	24	2695.5	9.1	−2
30.2	130	35	0.269	85.8	0.07	1.901	1.1	0.18462	0.57	2724	26	2694.8	9.4	−1
14.1	943	200	0.218	623.7	0.02	1.879	1.0	0.18450	0.17	2750	22	2693.7	2.7	−3
5.2	99	33	0.350	66.9	0.04	1.891	1.1	0.18435	0.50	2736	25	2692.4	8.2	−2
147.2	187	51	0.273	121.0	0.04	1.944	1.3	0.18428	0.34	2675	28	2691.8	5.5	1
42.1	129	40	0.303	86.3	0.16	1.890	1.2	0.18424	0.48	2737	27	2691.4	7.9	−2
11.1	197	60	0.312	131.1	0.05	1.906	1.1	0.18399	0.38	2719	25	2689.2	6.3	−1
Mixed analyses														
53.1	250	85	0.318	164.3	0.08	1.938	1.1	0.18327	0.35	2682	25	2682.7	5.7	0
47.1	837	241	0.278	545.5	0.03	1.933	1.0	0.18279	0.19	2688	22	2678.4	3.1	0
02.1	233	57	0.243	143.0	0.04	2.023	1.0	0.17368	0.33	2589	22	2593.4	5.4	0
Group 2 metamorphic (used for pooled maximum age)														
108.2	46	11	0.232	27.8	0.07	2.062	1.4	0.17095	0.71	2549	30	2567	12	1
51.1	73	22	0.283	44.1	0.10	2.069	1.2	0.17088	0.68	2542	25	2566	11	1
11.2	171	71	0.419	108.6	0.04	2.025	1.1	0.17079	0.40	2587	23	2565.4	6.7	−1
48.2	115	35	0.291	71.6	0.08	2.002	1.2	0.17057	0.52	2611	26	2563.2	8.7	−2
31.1	61	16	0.266	37.1	–	2.054	1.2	0.17043	0.82	2557	26	2562	14	0
22.1	139	32	0.227	84.5	0.11	2.030	1.1	0.17040	0.46	2582	24	2561.5	7.7	−1
101.1	59	12	0.207	34.9	0.07	2.067	1.4	0.17027	0.73	2544	30	2560	12	1
3.2	101	11	0.108	57.9	0.09	2.104	1.3	0.16989	0.53	2507	27	2556.5	8.9	2
18.1	133	34	0.254	81.0	0.06	2.033	1.1	0.16936	0.57	2579	23	2551.3	9.6	1
51.2	194	82	0.412	120.6	0.06	2.062	1.1	0.16918	0.46	2549	23	2549.6	7.7	0

(continued)

Table 4. *(Continued)*

Sample[1] spot no.	U (ppm)	Th (ppm)	Th/U[2]	Pb (ppm)	$^{206}Pb_c$[3] %	Ratios[4] $^{238}U/^{206}Pb$	±σ (%)	$^{207}Pb/^{206}Pb$	±σ (%)	Ages[4] $^{206}Pb/^{238}U$	±σ	$^{207}Pb/^{206}Pb$	±σ	Disc. %
29.2	97	28	0.280	58.7	0.09	2.055	1.1	0.16909	0.57	2556	24	2548.6	9.4	0
09.1	139	48	0.355	85.6	0.04	2.059	1.1	0.16898	0.44	2552	23	2547.5	7.4	0
147.1	41	8	0.192	24.3	0.06	2.075	1.5	0.16895	0.77	2536	32	2547	13	1
32.1	86	12	0.135	49.5	0.13	2.091	1.2	0.16882	0.73	2519	25	2546	12	1
78.2	57	11	0.193	34.1	0.04	2.040	1.4	0.16819	0.64	2572	30	2540	11	−2
55.1	60	17	0.260	35.4	0.48	2.108	1.3	0.16802	0.92	2503	27	2538	15	2
48.1	124	31	0.243	74.3	0.10	2.059	1.1	0.16770	0.52	2552	24	2534.8	8.8	−1
53.2	102	12	0.114	60.1	0.09	2.036	1.2	0.16760	0.58	2575	24	2533.9	9.7	−2
35.1	85	33	0.396	53.4	0.07	2.034	1.2	0.16744	0.64	2577	25	2532	11	−2
13.2	96	41	0.428	59.6	0.04	2.083	1.1	0.16744	0.55	2527	24	2532.2	9.3	0
Group 2 metamorphic (excluded)														
13.1	64	18	0.284	39.6	0.13	2.020	1.2	0.16650	0.68	2592	26	2523	11	−3
27.1	85	23	0.269	51.6	0.06	2.049	1.2	0.16612	0.61	2562	25	2519	10	2
33.1	72	20	0.271	43.4	0.07	2.044	1.3	0.16603	0.88	2568	27	2518	15	−2
60.1	94	26	0.274	55.8	–	2.082	1.2	0.16581	0.55	2529	25	2515.8	9.3	−1
63.2	61	15	0.251	36.6	–	2.055	1.5	0.16529	0.63	2556	32	2511	11	−2
Little Ramah Bay, sample L1487, n5549														
Xenocrystic														
04.1*	91	23	0.26	101.6	–	1.281	1.1	0.36180	0.32	3720	32	3757.4	4.9	1
Metamorphic														
08.1*	59	21	0.36	26.6	–	1.906	1.8	0.19302	0.91	2717	41	2768	15	2
05.2	23	11	0.46	16.4	–	1.886	1.6	0.19216	0.94	2743	36	2761	15	1
09.1*	54	19	0.37	24.0	0.04	1.931	1.8	0.19159	0.97	2687	42	2756	16	3
13.1*	59	22	0.39	27.0	0.13	1.883	1.8	0.1903	1.0	2739	42	2745	17	0
11.1*	261	83	0.33	119.0	0.47	1.880	1.2	0.19020	0.54	2753	29	2743.9	8.9	0
07.1*	52	13	0.26	23.7	0.20	1.902	1.9	0.1898	1.0	2725	43	2740	17	1
05.1*	59	20	0.35	28.0	0.06	1.815	2.9	0.18973	0.87	2827	69	2740	14	−4
03.2	25	11	0.45	17.6	–	1.898	1.6	0.1889	1.0	2728	35	2733	16	0
10.1*	72	14	0.19	32.8	0.06	1.891	1.7	0.18872	0.85	2739	39	2731	14	0
03.1*	57	16	0.29	25.9	0.14	1.898	1.7	0.18782	0.93	2730	40	2723	15	0
04.1*	63	22	0.36	29.2	0.15	1.840	1.7	0.18698	0.89	2801	40	2716	15	−4
Igneous														
04.2	667	412	0.64	768.0	0.02	1.302	1.1	0.33494	0.24	3673	31	3639.9	3.7	−1
19.1*	198	131	0.68	126.2	0.17	1.347	1.3	0.33493	0.38	3580	38	3639.8	5.8	2
18.1*	373	30	0.08	236.1	0.09	1.358	1.2	0.33215	0.26	3558	32	3627.0	4.0	3
01.1*	439	41	0.10	279.7	0.75	1.349	1.2	0.3258	0.74	3576	32	3598	11	1
02.1*	730	143	0.20	472.6	0.02	1.327	1.1	0.32434	0.36	3623	31	3590.6	5.5	−1
06.1*	495	41	0.09	309.8	–	1.371	1.1	0.32361	0.59	3533	31	3587.1	9.1	2
12.1*	350	40	0.12	215.4	0.19	1.397	1.2	0.32189	0.32	3483	32	3578.9	4.9	4
17.1*	195	90	0.48	117.2	0.11	1.425	1.3	0.3154	1.0	3436	36	3547	15	4
16.1*	535	79	0.15	321.4	0.02	1.429	1.1	0.31481	0.24	3420	31	3544.7	3.7	5
14.1*	693	83	0.12	420.5	0.03	1.416	1.1	0.31323	0.38	3447	30	3536.9	5.8	3
03.1	416	48	0.10	386.5	0.08	1.438	1.0	0.30600	0.42	3404	27	3500.9	6.4	4
*	314	43	0.14	168.6	0.02	1.601	1.2	0.26401	0.34	3131	30	3270.8	5.4	5
02.1	284	100	0.28	212.1	0.33	1.749	1.4	0.22670	0.58	2915	34	3028.9	9.3	5
02.2	366	142	0.35	273.5	0.11	1.769	1.0	0.22169	0.53	2888	23	2993.0	8.6	4
Discordant														
01.1	1382	321	0.19	1017.5	0.07	1.793	1.0	0.25996	0.13	2857	24	3246.4	2.0	15
Little Ramah Bay, sample L1488–89, n5550–n5551														
Metamorphic														
07.2	254	23	0.09	164.3	0.05	1.884	0.99	0.19208	0.30	2745	22	2760.1	5.0	1
04.2	614	51	0.08	400.0	0.03	1.863	1.0	0.19096	0.18	2770	23	2750.5	2.9	−1
05.1	151	86	0.58	108.5	0.25	1.881	1.1	0.19050	0.38	2748	24	2746.5	6.2	0
04.1	373	128	0.32	245.5	0.68	1.948	1.1	0.19035	0.41	2671	24	2745.2	6.7	3
02.2	73	53	0.73	53.5	0.29	1.905	1.2	0.18944	0.55	2720	26	2737.3	9.1	1
05.2	70	45	0.63	47.9	0.40	1.991	1.4	0.18933	0.63	2624	29	2736	10	5
Little Ramah Bay, sample L1490, n5552														
Metamorphic														
03.1	51	17	0.33	35.6	0.11	1.856	1.2	0.19292	0.67	2779	27	2767	11	−1
07.1	16	4	0.28	10.6	–	1.864	1.8	0.1923	1.5	2768	40	2762	24	0
01.2	56	18	0.33	38.0	–	1.900	1.2	0.19082	0.60	2726	26	2749.2	9.8	1

(continued)

Table 4. *(Continued)*

Sample[1] spot no.	U (ppm)	Th (ppm)	Th/U[2]	Pb (ppm)	$^{206}Pb_c$[3] %	Ratios[4]				Ages[4]				Disc. %
						$^{238}U/^{206}Pb$	±σ (%)	$^{207}Pb/^{206}Pb$	±σ (%)	$^{206}Pb/^{238}U$	±σ	$^{207}Pb/^{206}Pb$	±σ	
06.2	75	28	0.38	51.4	0.11	1.877	1.1	0.19081	0.65	2753	25	2749	11	0
08.3	40	12	0.29	26.8	–	1.897	1.5	0.19032	0.71	2730	33	2745	12	1
02.2	107	47	0.44	75.0	0.06	1.870	1.1	0.18922	0.51	2762	24	2735.4	8.3	−1
08.2	103	44	0.42	70.9	0.38	1.898	1.1	0.18915	0.48	2729	24	2734.8	7.9	0
04.2	13	3	0.24	9.1	0.34	1.840	1.8	0.1891	1.3	2798	41	2734	22	−3
08.1	68	25	0.34	45.3	0.10	1.916	1.2	0.18908	0.57	2707	25	2734.2	9.3	1
04.1	69	25	0.37	47.2	0.10	1.882	1.2	0.18900	0.56	2747	26	2733.5	9.2	−1
04.2	50	17	0.32	33.6	0.10	1.913	1.3	0.18728	0.70	2710	28	2718	11	0
07.2	10	3	0.27	6.5	–	1.861	2.2	0.1872	1.4	2772	50	2717	24	−2
05.2	11	3	0.25	7.6	–	1.866	1.9	0.1842	1.4	2767	44	2691	22	−3
Reichel Head, sample L1491, n5553														
Xenocrystic														
07.1	77	31	0.42	88.2	0.08	1.279	1.2	0.36038	0.55	3725	34	3751.5	8.4	−1
02.1*	290	74	0.26	200.0	0.04	1.246	1.2	0.36156	0.27	3801	36	3756.4	4.1	−1
Igneous														
02.2*	503	238	0.49	334.4	0.18	1.292	1.1	0.3540	0.63	3702	34	3724	10	1
01.1	192	97	0.51	226.2	0.02	1.258	1.2	0.35340	0.28	3771	34	3721.7	4.2	2
01.1*	137	21	0.16	91.8	0.02	1.285	1.4	0.3517	0.95	3710	40	3714	14	0
03.1*	302	159	0.54	206.2	0.04	1.258	1.2	0.35115	0.53	3776	35	3712.0	8.1	−2
08.1	390	57	0.14	423.8	0.04	1.276	1.1	0.34958	0.28	3730	31	3705.2	4.3	1
Excluded														
03.2*	187	85	0.47	124.3	0.05	1.294	1.3	0.34739	0.59	3696	38	3695.6	8.9	0
05.1*	488	99	0.21	313.4	0.21	1.337	1.1	0.3457	0.72	3600	33	3688.3	11	3
07.1*	196	81	0.42	123.5	0.04	1.365	1.3	0.34290	0.36	3544	37	3675.7	5.5	5
09.1*	180	144	0.82	114.7	0.02	1.349	1.7	0.34138	0.33	3582	51	3669.0	5.1	3
18.1*	651	9	0.01	413.3	0.39	1.353	1.1	0.33501	0.53	3568	30	3640.1	8.2	3
08.1*	710	71	0.10	371.7	0.77	1.640	1.1	0.28285	0.27	3067	27	3378.7	4.2	11
Reichel Head, sample L1492, n5547														
Detrital														
04.1*	91	42	0.47	53.0	0.22	1.473	2.8	0.2659	2.8	3348	76	3282	43	−2
03.1*	156	84	0.56	86.3	0.06	1.550	1.9	0.2578	1.6	3212	50	3233	25	1
01.1	139	50	0.36	122.9	–	1.534	1.2	0.2563	1.0	3235	31	3224	16	0
02.1*	158	80	0.53	89.8	0.07	1.510	1.3	0.2555	1.5	3284	36	3219	23	−2
02.2	204	82	0.41	177.7	0.04	1.569	1.2	0.25392	0.26	3179	30	3209.4	4.1	1
05.1	114	57	0.47	95.6	–	1.639	1.1	0.2396	0.80	3071	27	3117	13	2
02.1	104	36	0.32	82.6	0.07	1.670	1.5	0.2329	1.1	3025	36	3072	18	2
01.2	295	53	0.17	221.9	0.03	1.697	1.2	0.2284	0.95	2986	30	3041	15	2
01.1*	86	37	0.45	42.2	0.13	1.753	1.6	0.2163	2.3	2916	39	2953	37	2
Metamorphic														
04.1	390	2	0.00	247.3	0.04	1.879	1.0	0.19110	0.27	2750	23	2751.6	4.5	0
03.1	663	4	0.01	423.7	0.01	1.864	0.96	0.19000	0.20	2769	22	2742.1	3.3	−1
04.2	1144	13	0.01	730.2	0.04	1.866	1.0	0.18895	0.14	2766	23	2733.1	2.2	−1
05.2	335	2	0.00	213.1	0.05	1.871	1.1	0.18869	0.26	2760	25	2730.8	4.2	−1
06.2	588	14	0.02	373.8	0.02	1.876	1.0	0.18796	0.19	2754	23	2724.4	3.1	−1
03.2	332	2	–	–	0.10	1.943	1.0	0.18732	0.26	2677	23	2718.8	4.3	2
Reichel Head, sample L1493, n5548														
Xenocrystic														
03.2	732	113	0.14	756.0	0.80	1.341	1.03	0.34695	0.17	3591	28	3693.6	2.7	4
Metamorphic grains														
04.1	524	87	0.16	344.4	0.03	1.877	1.00	0.18972	0.20	2753	22	2739.8	3.3	−1
05.2	338	133	0.40	229.8	0.11	1.909	0.96	0.18862	0.26	2715	21	2730.2	4.2	1
05.1	609	98	0.16	391.6	0.04	1.915	0.98	0.18719	0.19	2708	22	2717.7	3.1	0
02.2	471	58	0.12	306.3	0.04	1.878	0.95	0.18711	0.28	2752	21	2716.9	4.6	−2
03.2	377	53	0.14	243.4	0.23	1.895	1.00	0.18621	0.25	2732	22	2709.0	4.1	−1

[1]sample labels include SIMS data from John deLaeter Centre (*) and NordSIMS (n####).
[2]Th/U ratios presented are calculated from measured Th and U oxides.
[3]Percentage of common ^{206}Pb in measured ^{206}Pb, calculated from the ^{204}Pb signal assuming a present-day Stacey & Kramers (1975) model terrestial Pb-isotope composition.
[4]Values corrected for common Pb.
Disc. % = (1-($^{206}Pb/^{238}Pb$ age)/($^{207}Pb/^{206}Pb$ age))*100

high-grade metamorphic conditions. Cores having euhedral, graduated and/or oscillatory growth zoning, typical of crystallization from an evolving magma, were found in all samples except L1453 (Hebron Fjord) and L1490 (Little Ramah Bay), the latter two having rounded or irregular cores without distinct growth zoning. Sub-grain domains of zircon with features typical of growth during metamorphism were targeted for spot analysis in all samples, and zircon grains with magmatic growth features were targeted in samples L1412 (near St Johns Harbour), L1414A/B (Dog Island), L1487 (Little Ramah Bay) and L1491 (Reichel Head). Isotopic U–Pb data (Table 4) are presented in Tera–Wasserburg concordia plots (Fig. 5) along with $^{207}Pb/^{206}Pb$ mean ages for concordant populations and Model 1 discordia intercept ages for linear arrays. Older outliers from rounded or irregular cores, which are interpreted as xenocrystic or inherited zircon, were not included in the calculation of ages and statistics from the identified populations. For cores and grains with growth zoning characteristic of igneous zircon, Model 1 discordia chords were calculated with forced lower intercepts of 2720 ± 50 Ma, approximating the time period within which granulite-facies gneisses were estimated to have formed from older magmatic protoliths in the Saglek Block (Kusiak *et al.* 2018, and references therein). Statistical test values (mean square of weighted deviates; MSWD) and other details are provided with the concordia plots in Figure 5.

For andesitic orthogneiss L1487 and trondhjemitic orthogneiss L1491, discordia chords yield upper intercept ages of 3664 ± 35 Ma and 3715 ± 26 Ma, respectively. The latter includes five concordant data with a mean $^{207}Pb/^{206}Pb$ age of 3714 ± 11 Ma. Data from zircon in trondhjemitic orthogneiss L1414B spread between *c.* 3650 and 3590 Ma. Mean $^{207}Pb/^{206}Pb$ ages were also derived from igneous zircon in meta-trondhjemite layer L1414A (2749 ± 3 Ma) and meta-monzonite L1412 (2547 ± 3 Ma). In all cases, the estimates are interpreted as the time of crystallization of igneous protoliths, with the exception of L1414B; in that sample, the cluster of analyses at *c.* 3590 Ma can be interpreted as a maximum age only for the protolith, assuming that they were not disturbed by later metamorphism. Igneous zircon from metapelite L1492 yielded scattered ages between *c.* 3280 and 2950 Ma, which are interpreted as dating detrital sources for the metasediment, although here again, the possibility of disturbance at *c.* 2.7 Ga cannot be discounted.

Zircon with metamorphic morphologies, either as rims with discordant boundaries to cores or as distinctly equant rounded and sector-zoned grains, yielded statistically valid (MSWD ≤ 1.3) mean $^{207}Pb/^{206}Pb$ ages for samples of andesitic orthogneiss L1487 (2742 ± 8 Ma), trondhjemitic orthogneiss L1488 (2750 ± 7 Ma) and mafic granulite L1490 (2739 ± 9 Ma). Slightly more scattered data were derived from metapelite L1492 (*c.* 2750–2720 Ma) and metagranite L1493 (*c.* 2740–2710 Ma). Two data from light-CL rims in zircon from sample L1414A yielded *c.* 2710 Ma ages. Together, these data from six samples are interpreted as dating zircon growth during high-*T* metamorphism between *c.* 2750 and 2710 Ma. The dataset from mafic granulite sample L1453 is more complex, with 51 analyses from unzoned, concentric and sector-zoned grains and cores ranging between *c.* 2740 and 2680 Ma (group 1 ages, Fig. 5), and 25 data from unzoned or gradationally zoned rims ranging between *c.* 2570 and 2510 Ma (group 2 ages). Analyses in group 1 record variable U contents (Fig. 5), whereas those from group 2 have uniformly low U contents. The groups represent periods of zircon growth during two separate metamorphic events. To better define the gap in time between the events, subsets of statistically equivalent data were extracted from the youngest ages in group 1 and the oldest ages in group 2. The 42 youngest out of 51 data in group 1 yield a mean $^{207}Pb/^{206}Pb$ age of 2702 ± 2 Ma, and the 20 oldest data out of 25 in group 2 yield a mean $^{207}Pb/^{206}Pb$ age of 2551 ± 6 Ma. These mean ages provide statistically robust estimates for the minimum age of zircon growth in the first metamorphic event, and the maximum age of growth in the second, respectively.

In situ *monazite dating*

To constrain the timing of mineral growth in high-grade metamorphic assemblages, plugs containing monazite and surrounding minerals were drilled from polished thin sections, mounted and analysed by secondary ion mass spectrometry (SIMS; Table 5, Fig. 5). Monazite in andesitic orthogneiss L1487 occurs as xenoblastic grains in a granoblastic assemblage that is strongly retrogressed, as described by Kusiak *et al.* (2018). Owing to the marginal alteration of monazite grains in thin section (Fig. 6a), data were also taken from unaltered fragments of monazite separated from the orthogneiss and mounted in a polished epoxy plug. Excluding three slightly younger, discordant data points, 12 analyses from a combination of grains in drilled thin sections and separates yielded a mean $^{207}Pb/^{206}Pb$ age of 2709 ± 14 Ma. Monazite in metapelite sample L1492 is unaltered and has polygonal grain boundaries with other metamorphic phases (Fig. 6b), and yields a mean $^{207}Pb/^{206}Pb$ age of 2727 ± 6 Ma. Ages were also collected from each part of metavolcanic rock L1458 (A, B and C). Two 10 µm wide monazite inclusions in garnet porphyroblasts from the garnet–biotite-rich part (L1458B) yield spot ages of *c.* 2680 and *c.* 2670 Ma. Monazite occurs more abundantly in association with garnet-leucosome L1458C, in which millimetre-scale preferentially aligned inclusions in garnet poikiloblasts are parallel to S_3 defined by biotite inclusions (Fig. 6c). Four inclusions of monazite yield ages that range from 2550 to 2510 Ma. Excluding the two oldest analyses, nine data yield a mean $^{207}Pb/^{206}Pb$ age of 2522 ± 7 Ma, which can be considered as a robust statistical minimum age for the period of metamorphism. Age data were also obtained from monazite separated from the orthopyroxene-rich part (L1458A) and yielded a mean $^{207}Pb/^{206}Pb$ age of 2551 ± 5 Ma. Mean ages from samples L1487 and L1492 are attributed to monazite growth during the first period of high-*T* metamorphism. Monazite from sample L1458, dated as inclusions in garnet from parts B and C, indicates multiple stages of mineral growth. Those grains present in cross-cutting garnet-leucosome (L1458C) fall within the second period of mineral growth at 2.5 Ga identified in zircon from other samples in this study, as does monazite in the matrix of part A. The two monazite inclusions in the garnet–biotite-rich part (B) fall between the two stages of zircon growth in other samples, but agree with some monazite age estimates obtained by Kusiak *et al.* (2018). This may be an indication of monazite growth and/or disturbance continuing after 2700 Ma, but as a separate generation from the second stage of growth from 2550 to 2510 Ma.

Discussion

Significance and correlation between Labrador and Greenland

The new results from monazite and zircon associated with metamorphic assemblages and deformation fabrics, especially where supported by dating structurally constrained meta-granitoids, provide evidence of two distinct high-temperature tectonothermal events: at 2750–2700 Ma and 2550–2510 Ma (Fig. 7). The separation of the two episodes of high-*T* mineral growth is clearer than that observed in EMP monazite dating by Kusiak *et al.* (2018). There is evidence of partial melting and crystallization of anatectic melt in both the earlier and later stages of each of the events. Therefore, the growth of zircon and monazite after 2550 Ma is probably not due to the 'thermal effects' of granitic emplacement, as suggested by Schiøtte *et al.* (1992); rather, it is more likely that

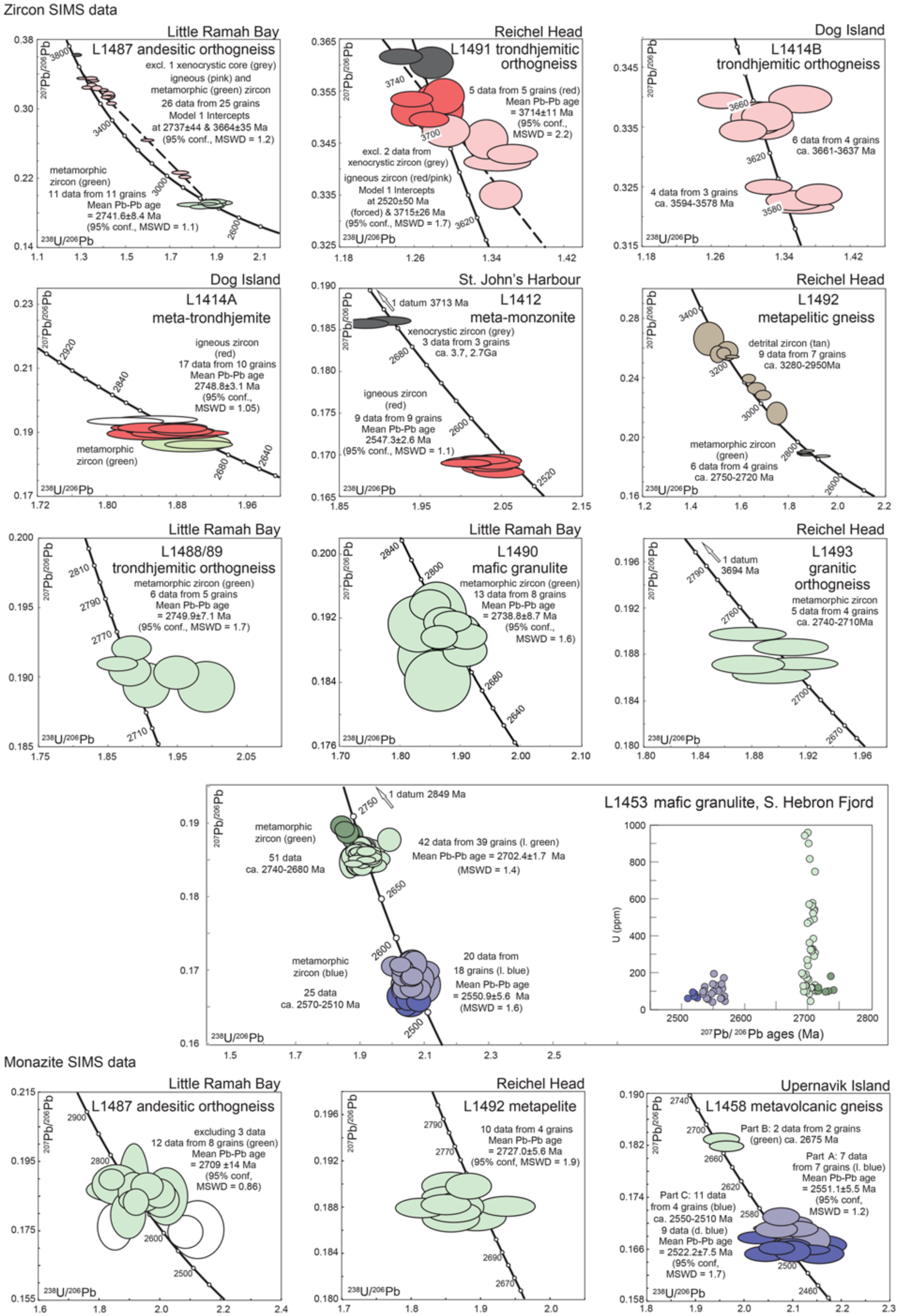

Fig. 5. Tera–Wasserburg concordia plots of SIMS age data from zircon and monazite. Spot ages represented by error ellipses are colour-coded according to type: green, *c.* 2.7 Ga metamorphic; blue, *c.* 2.5 Ga metamorphic; red or pink, igneous; grey, xenocrystic or inherited; tan, detrital.

Table 5. *Monazite SIMS U–Th–Pb data*

Sample and spot no.	U (ppm)	Th (ppm)	Th/U[1]	$^{206}Pb_c$[2] %	Ratios[3]				Age[3]		Disc. %
					$^{238}U/^{206}Pb$	±σ (%)	$^{207}Pb/^{206}Pb$	±σ (%)	$^{207}Pb/^{206}Pb$	±σ	
Upernavik Island, sample L1458											
Part A, mineral separate, metamorphic											
08.1	511	54753	107	0.055	2.075	1.2	0.17103	0.53	2567.7	8.9	1
05.1	726	45827	63	0.048	2.094	1.4	0.17001	0.45	2557.7	7.6	2
02.1	4733	41569	9	0.005	2.073	1.7	0.16925	0.28	2550.2	4.8	0
09.1	701	32556	46	0.039	2.107	1.4	0.16916	0.47	2549.4	7.8	2
03.1	562	45054	80	0.054	2.082	1.4	0.16887	0.51	2546.5	8.5	1
01.1	732	36398	50	0.024	2.108	1.5	0.16876	0.44	2545.4	7.4	2
06.1	501	56462	113	0.125	2.138	1.2	0.1675	0.82	2533	14	2
Part B, inclusions in garnet, metamorphic											
14.1	1918	46264	24	0.030	1.953	1.3	0.18296	0.35	2679.9	5.7	1
15.1	5811	31893	5	0.016	1.964	1.2	0.18187	0.30	2670.0	4.9	1
Part C, inclusions in garnet, metamorphic, used for pooled minimum age											
11.2	607	61328	101	0.048	2.1165	1.2	0.1681	0.52	2538.5	8.7	2
12.3	1829	53425	29	0.095	2.0273	1.3	0.1678	0.37	2536.1	6.1	−2
16.1	1916	42995	22	0.038	2.1538	1.7	0.1667	0.61	2525	10	3
11.3	674	58064	86	0.088	2.0957	1.3	0.1664	0.51	2521.8	8.6	0
12.1	3628	49372	14	0.041	2.0667	1.2	0.1662	0.40	2520.2	6.7	−1
12.2	4673	54453	12	0.019	2.1335	1.3	0.1659	0.30	2517.0	5.0	2
16.2	662	43635	66	0.662	2.0992	1.2	0.1657	0.64	2515	11	0
10.1	549	54711	100	0.320	2.1545	1.5	0.1654	0.60	2511	10	2
11.4	884	58627	66	0.087	2.0434	1.4	0.1653	0.46	2511.0	7.8	−2
Excluded from pooled age											
12.4	809	55352	68	0.037	2.1093	1.3	0.1692	0.64	2550	11	2
11.1	596	63598	107	–	2.0661	1.4	0.1691	0.51	2548.8	8.5	0
Little Ramah Bay, sample L1487											
Metamorphic											
01.1	167	22472	134	0.49	1.841	1.5	0.1898	1.0	2741	17	−2
03.1	116	10079	87	0.47	1.914	1.7	0.1889	3.9	2733	65	1
01.2	68	16731	248	1.22	1.857	2.8	0.1884	2.0	2728	33	−2
09.1	86	3171	37	0.32	1.958	1.8	0.1879	1.4	2724	23	2
08.1	78	1982	25	0.13	1.859	3.6	0.1868	1.2	2714	20	−2
09.2	86	2698	31	0.35	1.913	1.7	0.1862	2.0	2709	33	0
02.1	103	2487	24	0.60	1.997	1.7	0.1859	1.5	2706	24	3
07.1	53	9264	174	2.02	2.021	2.3	0.1850	2.9	2698	49	4
08.2	92	2666	29	0.71	2.005	1.9	0.1839	1.7	2688	29	3
05.2	173	19891	115	0.66	1.933	2.3	0.1838	1.2	2687	20	0
07.2	262	14716	56	0.71	1.921	1.4	0.1834	1.4	2684	23	−1
10.1	62	9731	158	2.00	1.895	2.0	0.1797	2.5	2650	42	−3
Discordant, outliers											
10.2	62	10591	171	1.75	1.852	2.1	0.1763	2.5	2618	42	−6
04.1	114	8348	73	0.52	2.124	2.7	0.1754	3.1	2610	52	5
02.2	85	2027	24	0.76	2.084	1.8	0.1748	1.8	2604	30	3
Reichel Head, sample L1492											
Metamorphic											
02.2	3099	33150	11	0.009	1.857	1.5	0.18987	0.41	2741.0	6.7	−1
04.2	3489	27359	8	0.012	1.882	1.2	0.18983	0.39	2740.7	6.4	0
04.4	2939	34681	12	–	1.856	1.4	0.18893	0.31	2732.9	5.1	−2
03.2	3028	35113	12	0.000	1.850	1.3	0.18824	0.30	2726.9	5.0	−2
02.3	3292	34864	11	–	1.937	1.4	0.18810	0.30	2725.6	5.0	2
04.3	2725	33525	12	0.020	1.868	1.3	0.18804	0.45	2725.1	7.5	−1
04.1	3695	27895	8	0.000	1.815	1.3	0.18795	0.30	2724.3	4.9	−4
03.1	2548	33441	13	0.019	1.861	1.4	0.18760	0.31	2721.2	5.2	−2
01.1	3147	31700	10	–	1.894	1.5	0.18716	0.42	2717.4	6.9	−1
02.1	3391	28271	8	0.018	1.857	1.5	0.18701	0.40	2716.1	6.6	−2

[1]Th/U ratios presented are calculated from measured Th and U oxides.
[2]Percentage of common ^{206}Pb in measured ^{206}Pb, calculated from the ^{204}Pb signal assuming a present-day Stacey & Kramers (1975) model terrestial Pb-isotope composition.
[3]Values corrected for common Pb.
Disc. % = (1-($^{206}Pb/^{238}Pb$ age)/($^{207}Pb/^{206}Pb$ age))*100.

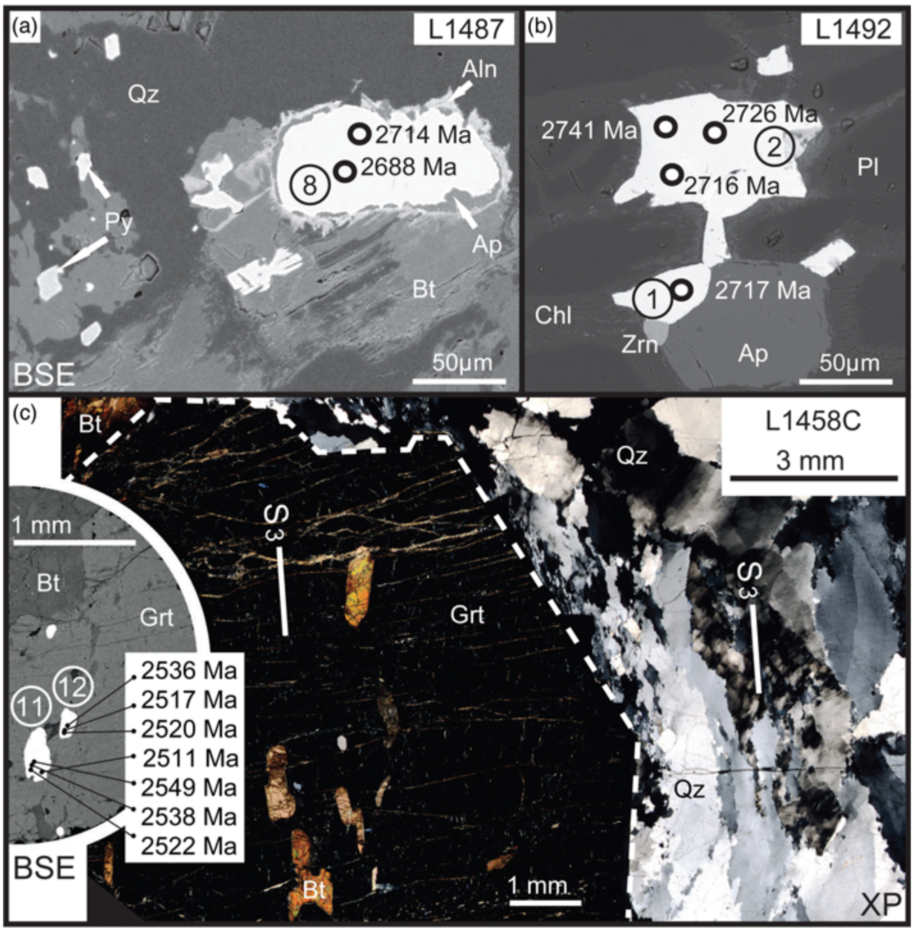

Fig. 6. Microimaging of monazite dated *in situ* by SIMS. In backscattered electron (BSE) images, monazite appears white, with grains analysed for isotopic dating identified by numbers in circles. (**a**) Grain 8 in sample L1487 of andesitic orthogneiss, Little Ramah Bay, with thin dual corona of apatite and allanite or epidote against enclosing assemblage of biotite (altered to chorite), plagioclase, quartz and pyrite. BSE image, WOV 0.3 mm. (**b**) Grains 1 and 2 in sample L1492 of metapelite, Reichel Head, with polygonal and interstitial relationships to plagioclase, apatite and zircon. Chlorite replaces biotite. BSE image, WOV 0.2 mm. (**c**) S_3-aligned grains 11 and 12 in garnet idioblast, sample L1458C of neosome vein in metavolcanic gneiss, Upernavik Is. Biotite and monazite grains included in garnet are aligned with S_3; marginal recrystallization in quartzose neosome and orthogonal fracturing in idioblastic garnet indicate deformation after crystallization of melt, possibly during late D_3. Crossed polars, WOV 12 mm. Inset: *in situ* BSE image of disc drilled for SIMS analysis (compare with Fig. 2h). Qz, quartz; Py, pyrite; Bt, biotite; Aln, allanite; Ap, apatite; Zrn, zircon; Pl, plagioclase; Chl, chlorite; Grt, garnet.

tectonothermal activity is the progenitor of granitic melts that were emplaced both during and after high-strain deformation. These include the *c.* 2530 Ma major granitic stockworks described by Baadsgaard *et al.* (1979) on the coast and islands outside Saglek Bay. A re-examination of localities in which *c.* 2.5 Ga magmatism and mineral growth occurs shows that such ages are scattered along the Saglek Block from Saglek Bay to Nain, and on both sides of the Handy Fault (Fig. 8). Further north there is a lack of data; however, zircon growth during metamorphic events at *c.* 2.7 and 2.5 Ga have been recognized by Scott (1995) in meta-tonalites at Home and Avayalik Islands, which may be part of the Nain Province. Nevertheless, it is likely that the effects of the 2.5 Ga event increase towards the south and east, as such ages were also obtained from zircon and monazite in drill-core samples taken *c.* 40 km outside Saglek Bay (Wasteneys *et al.* 1996; see Fig. 8). In that study, the authors hypothesized a north–south-trending tectonic boundary between the Saglek and Hopedale blocks that extends southward from offshore of Saglek Bay to the coast near Okak Island. The Saglek Block comprises *c.* 3.7 Ga protoliths metamorphosed at *c.* 2.7 Ga and the Hopedale Block contains *c.* 3.2 Ga protoliths metamorphosed at *c.* 2.5 Ga. Anomalies, such as the presence in the Saglek Block of the *c.* 3.2 Ga Lister gneiss, from which a migmatized sample yielded *c.* 2.5 Ga zircon and titanite, have been attributed to tectonic intercalation of fragments of the Hopedale block within the Saglek Block at *c.* 2.5 Ga (Schiøtte *et al.* 1992; Wasteneys *et al.* 1996). However, the presence of *c.* 2680 Ma granitoid sheets cutting folded and metamorphosed Lister gneiss constrains gneiss formation to *c.* 2.7 Ga (Schiøtte *et al.* 1989). This, along with the evidence for *c.* 2.7 and *c.* 2.5 Ga metamorphism in samples from the Saglek area in our study and in that of Kusiak *et al.* (2018), does not contradict the terrane boundary proposed by Wasteneys *et al.* (1996), but does suggest that the assembly of the Saglek and Hopedale blocks was earlier than *c.* 2.5 Ga.

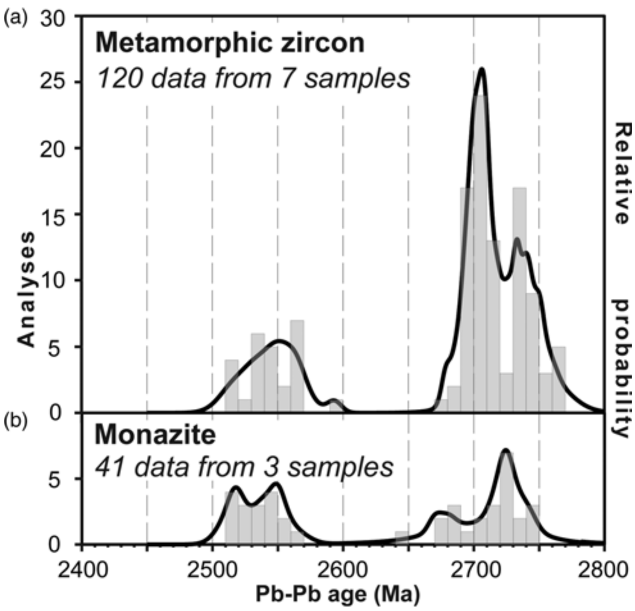

Fig. 7. Histogram of combined $^{207}Pb/^{206}Pb$ spot ages from SIMS analysis of metamorphic zircon and monazite in multiple samples. (**a**) L1412, L14014A-B, L1453, L1487, L1488/89, L1492; (**b**) L1458, L1487, L1492.

The late Archean metamorphic events and the assembly of two different crustal blocks in northern Labrador may be analogous to the juxtaposition of terranes having differing structural and metamorphic histories in the Archean of southwestern Greenland

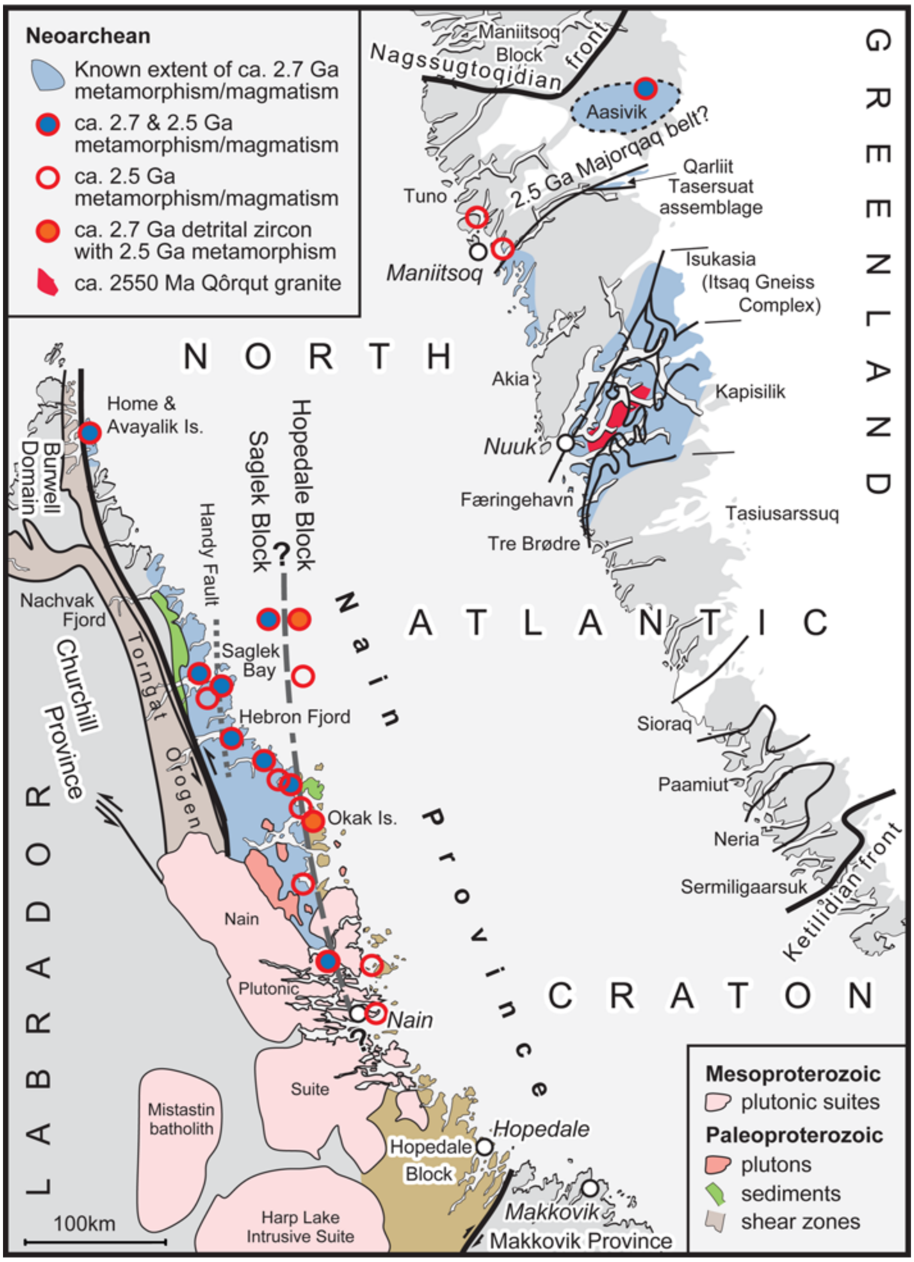

Fig. 8. Reconstruction of the western part of the North Atlantic Craton before the opening of the Labrador Sea, modified after St-Onge *et al.* (2009), and showing the location of magmatic and metamorphic mineral ages (U–Pb zircon, monazite and titanite ages, and K–Ar hornblende ages) that fall within the *c.* 2.7 and 2.5 Ga events, and the approximate known extent of *c.* 2.7 Ga metamorphism in the Nain Province and southwestern Greenland. A hypothetical boundary between the Hopedale and Saglek blocks, slightly modified from that proposed by Connelly & Ryan (1996) and Wasteneys *et al.* (1996), is shown by dashed line, parallel to the Handy Fault. Terranes in southwestern Greenland (bound by black lines) and the extent of Proterozoic orogenic fronts (thick black lines) are from Henriksen *et al.* (2009). Age data are from Wanless *et al.* (1970, 1974), Barton (1975), Collerson *et al.* (1982), Schiøtte *et al.* (1990, 1992), Scott (1995), Connelly & Ryan (1996), Wasteneys *et al.* (1996), Wendt & Collerson (1999), Connelly (2001), Rosing *et al.* (2001), Nutman *et al.* (2004, 2011, 2013), Krogh & Kamo (2006), Nutman & Friend (2007), Næraa *et al.* (2014), Dyck *et al.* (2015), Dziggel *et al.* (2017), Kirkland *et al.* (2018), Kusiak *et al.* (2018) and Sałacińska *et al.* (2018).

(Nutman & Friend 2007; Friend & Nutman 2019). Major late Archean terrane boundaries along the coast of southwestern Greenland tend to run NE into the glacial cap, rather than following the general north–south trend of gneisses in the Saglek area. *Circa* 2.8–2.7 Ga high-grade metamorphism that strongly affects the Nain Province also does so in the vicinity of Nuuk, with grade decreasing towards the east (e.g. Nutman & Friend 2007; Dziggel *et al.* 2017). This part of the North Atlantic Craton contains a complex mixture of Eoarchean and Paleoarchean terranes, and Mesoarchean arc assemblages, and has many similarities in timing and composition to the gneisses of the Saglek Block. The extensive *c.* 2560 Ma Qôrqut Granite Complex that intrudes gneisses inland from Nuuk (Nutman *et al.* 2011; Næraa *et al.* 2014) is a potential correlative of syn- to late-D_3 magmatism in the Saglek block, as marginal tectonic reworking of the Qôrqut has been observed (Nutman *et al.* 2011). However, no significant granite metamorphic event at *c.* 2.5 Ga is recognized in this part of Greenland. Some 100 km to the north, dating of *c.* 2.5 Ga metamorphic monazite in gneisses near Maniitsoq and inland led Dyck *et al.* (2015) to define the Majorqaq Belt, a NE-trending mobile belt between the main 2.7 Ga assembled part of the North Atlantic Craton and the Mesoarchean Maniitsoq block further north. Dyck *et al.* (2015) suggested that the belt resulted from the collision of the Maniitsoq block subsequent to southward subduction of an ocean basin beneath the North Atlantic Craton, and that the Qôrqut Granite Complex is the product of slab dewatering. The Majorqaq Belt might well correlate with *c.* 2.5 Ga tectonothermal activity in the Saglek Block. In this case, the Qôrqut Granite Complex would correlate well with large plutons of the same age found to the south of Saglek in the Okak area (Schiøtte *et al.* 1992). Indeed, the Maniitsoq block itself was subjected to marginal reworking to the north by Paleoproterozoic tectonism, similar to the northern and western margins of the Nain Province (St-Onge *et al.* 2009). However, there is a lack of data from the Labrador coast north of Ramah Bay that would allow any clear correlation to be made with the hypothesized ‘Majorqaq’ Belt. In addition, this would dissociate the Eoarchean Uivak gneiss from terranes of similar age in the Itsaq Gneiss Complex (Fig. 8). The latter has complicated ductile structural relationships with Paleo- to Mesoarchean terranes (Hoffmann *et al.* 2014). If such relationships are similarly complicated in the Saglek Block, the intercalation of older and younger crust there may also be a product of amalgamation at *c.*

2.7 Ga. A simpler correlation would place *c.* 2.5 Ga tectonothermal activity as a reworking of *c.* 2.7 Ga gneisses in association with the Okak and Qôrqut granitic complexes, on the eastern and southern margins of a composite Eoarchean–Mesoarchean continent. To test this hypothesis, geochronological work needs to be extended further north along the Labrador coast, and to little-studied parts of southwestern Greenland.

Conclusion

In situ U–Pb ion microprobe dating of monazite and sub-grain dating of zircon and monazite provide clear evidence of high-*T* metamorphism at both *c.* 2.7 and *c.* 2.5 Ga in the Saglek Block. Both events involved ductile deformation, with the former producing the dominant gneissosity in the Uivak and other gneisses, including supracrustal metasedimentary and metavolcanic varieties. The effects of tectonothermal activity at *c.* 2.7 Ga are widespread in the Saglek Block, as they are in the parts of southwestern Greenland conjugate to the Nain Province before the opening of the Labrador Sea. The known extent of *c.* 2.5 Ga high-*T* metamorphism and deformation is more limited, and may be restricted to reworking of the margins of the North Atlantic Craton in both Greenland and Labrador. However, given the emplacement of large amounts of *c.* 2.5 Ga granitoid in both Labrador and southwestern Greenland, it is possible that parts of the North Atlantic Craton were assembled at this time, involving the juxtaposition of pre-existing continental crust in Labrador (the Saglek and Hopedale blocks of the Nain Province) and Greenland (between the Maniitsoq block and others to the south). The evidence for late Neoarchean final assembly is still very limited, and will require extensive new geochronological studies in both Labrador and Greenland.

This study also provides zircon ages for the formation of supracrustal precursors to gneisses in the Saglek Block 30 km to the north of Saglek Bay. A protolith age of *c.* 3.7 Ga for andesitic orthogneiss at Little Ramah Bay is comparable with Eoarchean ages for the Uivak gneiss that have been well established by many earlier studies. *Circa* 3 Ga ages from detrital zircon in graphite-bearing metapelitic gneiss from Reichel Head are comparable with those obtained from similar gneiss at St John's Harbour, and support the conclusion of Whitehouse *et al.* (2019) that such graphite-bearing gneisses were not deposited at the beginning of the Archean, as proposed by Tashiro *et al.* (2017). These ages provide new evidence for the northward continuation of the Saglek Block, and demonstrate the potential for new discoveries of Eoarchean crust along the Labrador coast.

Acknowledgements Fieldwork was carried out with the permission and support of Parks Canada (special thanks go to D. Whitaker) and the Nunatsiavut Government. N. McNaughton, I. Fletcher and B. Rasmussen are thanked for assistance with monazite dating at the John de Laeter Centre, Curtin University, Australia. A. Gawęda of the Faculty of Earth Sciences, University of Silesia in Katowice, Poland, is thanked for assistance with whole-rock geochemical analysis. The staff of the Torngat Mountains Base Camp, and especially the boat pilots and bear guards who tirelessly supported and protected us in the field, are warmly thanked. Special thanks to B. Ryan for his thorough review that greatly improved the manuscript, and to Randall Parrish for his careful editorial handling.

Funding The lead author (D.J.D.) was supported by a Polish National Science Centre (NSC) POLONEZ Fellowship grant 2016/23/P/ST10/01214, funded through the EU H2020 research and innovation programme under MSCA grant agreement 665778. This research was also supported by NSC OPUS grant 2014/15/B/ST10/04245 to M.A.K.; grants to M.J.W. from the Knut and Alice Wallenberg Foundation (2012.0097) and the Swedish Research Council (2012-4370); and funding to S.A.W. from the Australian Research Council Centre of Excellence for Core to Crust Fluid Systems (CCFS). The NordSIMS facility operates as a Swedish national infrastructure under Swedish Research Council grant 2014-06375; this is NordSIMS contribution 611. Work by A.S. was supported by an ING-PAN internal project for young scientists (2016–2017).

Author contributions DJD: Conceptualization (Lead), Formal analysis (Equal), Writing – Original Draft (Lead); MAK: Conceptualization (Equal), Formal analysis (Equal), Writing – Original Draft (Supporting); SAW: Conceptualization (Equal), Data curation (Supporting), Writing – Review & Editing (Supporting); MJW: Conceptualization (Equal), Data curation (Supporting), Methodology (Supporting), Writing – Review & Editing (Supporting); AS: Formal analysis (Supporting); RK: Formal analysis (Supporting); PK: Formal analysis (Equal).

Appendix: Analytical protocols

Polished thin sections from all samples were prepared and examined by optical microscope and SEM at the John de Laeter Centre, Curtin University, Western Australia. For *in situ* monazite analysis (samples L1458 and L1487), 3 and 5 mm discs were drilled out of thin sections and mounted in epoxy discs. For mineral grain dating, samples were crushed and sieved, and then processed by wet panning, magnetic separation and hand picking to isolate zircon and monazite grains. The grains were mounted, along with reference materials, in epoxy discs that were then polished to expose the mid-sections of grains. All grains were imaged for internal structure before and after analysis using an SEM fitted with BSE and CL detectors. The mounts were cleaned and gold coated prior to analysis by SIMS.

Initial dating of mounted zircon grains was carried out by SHRIMP II at the John de Laeter Centre, Curtin University in Perth, Western Australia. A spot size of 20–25 µm was used with an O_2^- primary beam intensity of 3–4 nA. The secondary ion beam was focused through a 100 µm collector slit onto an electron multiplier to produce mass peaks with flat tops and a mass resolution (1% peak height) better than 5100 $M/\Delta M$. Data were collected in sets of six scans, with reference standards analysed after every five sample analyses. Count times per scan for Pb isotopes 204, background position 204.1, 206, 207 and 208, were 10, 10, 10, 30 and 10 s, respectively. U–Th–Pb ratios and absolute abundances were determined relative to the zircon reference standard BR266 (559 Ma, 903 ppm U; Stern (2001). Instrumental mass fractionation (IMF) of $^{207}Pb/^{206}Pb$ was monitored during each session by repeated analysis of the zircon reference standard OGC (Stern *et al.* 2009). No IMF correction was required because the measured values of OGC were in agreement with the reference value within 2σ uncertainty. Raw data were processed using the SQUID 2 add-in (v. 2.50.12.03.08) for Excel 2003 (Ludwig 2009) and plotted using the ISOPLOT 3.70 add-in of Ludwig (2001). Measured compositions were corrected for common Pb using measured ^{204}Pb and contemporaneous common Pb composition according to the terrestrial Pb evolution model of Stacey & Kramers (1975). Owing to the low proportion of common Pb detected in standards and samples (<1% of measured ^{206}Pb, as estimated from ^{204}Pb measurement), the choice of modelling age for common Pb composition did not have a statistically significant effect on age estimates. Mean ages are quoted with 95% confidence levels.

Further analysis of zircon in samples L1412, L1414, L1453, L1488-89, L1490, L1491, L1492 and L1493 was carried out by CAMECA IMS 1280 ion microprobe at the NordSIMS facility, Swedish Museum of Natural History, Stockholm. Protocols for U–Pb data closely follow published methods (Whitehouse & Kamber 2005). Zircon grains were analysed using a *c.* 15 µm, 6 nA O_2^- primary beam, and peak-hopping monocollection in an ion counting electron multiplier (EM) at a mass resolution of *c.* 5400 $M/\Delta M$. Reference material 91500 (1065 Ma, 80 ppm of U; Wiedenbeck *et al.* 1995) was used for calibration of Pb/U ratios using the Pb/UO v. UO_2/UO calibration protocol of Jeon & Whitehouse (2015). Common Pb was corrected using the ^{204}Pb counts assuming a present-day terrestrial Pb-isotope composition model (Stacey & Kramers 1975) following the rationale of Zeck & Whitehouse (1999) that this is largely surface contamination introduced during sample preparation and not common Pb residing in zircon and/or micro-inclusions. Very low amounts of common Pb were detected during the spot analyses with (<0.1% of total ^{206}Pb), in many cases below detection limit for ^{204}Pb based on the electron multiplier background. Where common Pb corrections were deemed necessary on the basis of measurable ^{204}Pb (>3× standard deviation on the average background), these were small and therefore insensitive to the precise composition of common Pb. Data reduction was performed using the NordSIMS-developed suite of software of M. J. Whitehouse. All ion microprobe data are quoted with 1σ analytical errors, whereas weighted mean and discordia intercept ages are quoted at 95% confidence levels, and include the decay-constant error of the concordia curve.

For *in situ* (i.e. within polished thin section) and grain mount monazite analysis, the SHRIMP II was operated with a primary beam of O_2^- ions focused through a 50 µm Köhler aperture to produce an oval 10 µm wide spot with a surface current of 0.2–0.4 nA. Secondary ionization was measured without energy filtering on a single electron multiplier on 13 mass stations from 202 ($LaPO_2$) to 270 (UO_2), with a mass resolution of >5200 for the latter. Secondary ion retardation was used to eliminate ion scatter. Mass stations 202 ($LaPO_2$), 203 ($CePO_2$), 205.9 ($NdPO_2$), 232 (Th), 244.8 (YCeO) and 264 (ThO_2) were analysed for matrix corrections and interference on ^{204}Pb, following the protocols outlined by Fletcher *et al.* (2010). Mass stations were measured through six cycles, with typical count times of 10 s per cycle for ^{204}Pb, background (at 204.04 a.m.u.) and ^{206}Pb, 30 s for ^{207}Pb and 5 s for ^{208}Pb. Reduction of raw data for standards and samples was performed using the SQUID 2.5 and Isoplot 3.70 add-ins for Microsoft Excel 2003 (Ludwig 2001, 2009). Age (^{206}Pb/^{238}U) and abundance of U were calibrated against reference monazite French (514 Ma; 1000 ppm U). High La and high Y–Nd–U standards Z2234 and Z2908, respectively, were used for matrix and interference corrections, following the method described by Fletcher *et al.* (2010). Corrections for common Pb on isotopic U/Pb values and ages were carried out with common Pb estimated from ^{204}Pb counts and the composition of Broken Hill lead.

For Zr-in-rutile thermometry, electron microprobe analysis was undertaken at the Electron Microprobe Laboratory, State Geological Institute of Dionýza Štúra, Bratislava, Slovakia, utilizing a Cameca SX-100 electron microprobe equipped with four wavelength-dispersive spectrometers. Large high-sensitivity, LPET and LLIF crystals and a conventional TAP crystal were used for analysis. Analytical conditions were chosen to balance the best analytical conditions against reasonable acquisition times. An accelerating voltage of 15 kV was used, with a probe current of 200 nA. Zirconium contents were calibrated against an in-house standard.

Scientific editing by Randall Parrish

Correction notice: The copyright has been updated to Open Access.

References

Baadsgaard, H., Collerson, K.D. & Bridgwater, D. 1979. The Archean gneiss complex of northern Labrador. 1. Preliminary U–Th–Pb geochronology. *Canadian Journal of Earth Sciences*, **16**, 951–961.

Barker, F. 1979. Trondhjemites: definition, environment and hypothesis of origin. *In*: Barker, F. (ed.) *Trondhjemites, Dacites and Related Rocks*. Elsevier, Amsterdam, 1–12.

Barton, J.M. 1975. The Mugford Group volcanics of Labrador: age, geochemistry and tectonic setting. *Canadian Journal of Earth Sciences*, **12**, 1196–1208, https://doi.org/10.1139/e75-109

Bridgwater, D. & Schiøtte, L. 1991. The Archaean gneiss complex of northern Labrador, a review of current results, ideas and problems. *Bulletin of the Geological Society of Denmark*, **39**, 153–166.

Bridgwater, D., Watson, J. & Windley, B.F. 1973. The Archaean craton of the North Atlantic region. *Philosophical Transactions of the Royal Society of London, Series A*, **273**, 493–512, https://doi.org/10.1098/rsta.1973.0014

Bridgwater, D., Collerson, K.D., Hurst, R.W. & Jesseau, C.W. 1975. *Field characters of the early Precambrian rocks from Saglek, Coast of Labrador*. Newfoundland Department of Energy, Mines and Resources, St John's.

Collerson, K.D. & Bridgwater, D. 1979. Metamorphic development of early Archaean tonalitic and trondhjemitic gneisses: Saglek area, Labrador. *In*: Barker, F. (ed) *Trondhjemites, Dacites, and Related Rock*. Elsevier, Amsterdam, 205–271.

Collerson, K.D., Kerr, A., Vocke, R.D. & Hanson, G.N. 1982. Reworking of sialic crust as represented in late Archaean-age gneisses, northern Labrador. *Geology*, **10**, 202–208, https://doi.org/10.1130/0091-7613(1982)10<202:ROSCAR>2.0.CO;2

Connelly, J.N. 2001. Constraining the timing of metamorphism: U–Pb and Sm–Nd ages from a transect across the Northern Torngat Orogen, Labrador, Canada. *Journal of Geology*, **109**, 57–77, https://doi.org/10.1086/317965

Connelly, J.N. & Ryan, B. 1996. Late Archean evolution of the Nain Province, Nain, Labrador: Imprint of a collision. *Canadian Journal of Earth Sciences*, **33**, 1325–1342, https://doi.org/10.1139/e96-100

Dyck, B., Reno, B.L. & Kokfelt, T.F. 2015. The Majorqaq Belt: A record of Neoarchaean orogenesis during final assembly of the North Atlantic Craton, southern West Greenland. *Lithos*, **220–223**, 253–271, https://doi.org/10.1016/j.lithos.2015.01.024

Dziggel, A., Kokfelt, T.F., Kolb, J., Kisters, A.F.M. & Reifenröther, R. 2017. Tectonic switches and the exhumation of deep-crustal granulites during Neoarchean terrane accretion in the area around Grædefjord, SW Greenland. *Precambrian Research*, **300**, 223–245, https://doi.org/10.1016/j.precamres.2017.07.027

Fletcher, I.R., McNaughton, N.J., Davis, W.J. & Rasmussen, B. 2010. Matrix effects and calibration limitations in ion probe U–Pb and Th–Pb dating of monazite. *Chemical Geology*, **270**, 31–44, https://doi.org/10.1016/j.chemgeo.2009.11.003

Friend, C.R.L. & Nutman, A.P. 2019. Tectono-stratigraphic terranes in Archaean gneiss complexes as evidence for plate tectonics: The Nuuk region, southern West Greenland. *Gondwana Research*, **72**, 213–237, https://doi.org/10.1016/j.gr.2019.03.004

Henriksen, N., Higgins, A.K., Kalsbeek, F., Christopher, T. & Pulvertaft, R. 2009. *Greenland from Archaean to Quaternary: Descriptive text to the 1995 Geological Map of Greenland 1:2500000*, 2nd edn. Survey of Denmark and Greenland Bulletin, **18**.

Hoffmann, J.E., Nagel, T.J., Münker, C., Næraa, T. & Rosing, M.T. 2014. Constraining the process of Eoarchean TTG formation in the Itsaq Gneiss Complex, southern West Greenland. *Earth and Planetary Science Letters*, **388**, 374–386, https://doi.org/10.1016/j.epsl.2013.11.050

Jeon, H. & Whitehouse, M.J. 2015. A critical evaluation of U–Pb calibration schemes used in SIMS zircon geochronology. *Geostandards and Geoanalytical Research*, **39**, 443–452, https://doi.org/10.1111/j.1751-908X.2014.00325.x

Kirkland, C.L., Yakymchuk, C., Hollis, J., Heide-Jørgensen, H. & Danišík, M. 2018. Mesoarchean exhumation of the Akia terrane and a common Neoarchean tectonothermal history for West Greenland. *Precambrian Research*, **314**, 129–144, https://doi.org/10.1016/j.precamres.2018.06.004

Komiya, T., Yamamoto, S. *et al.* 2015. Geology of the Eoarchean, >3.95 Ga, Nulliak supracrustal rocks in the Saglek Block, northern Labrador, Canada: The oldest geological evidence for plate tectonics. *Tectonophysics*, **662**, 40–66, https://doi.org/10.1016/j.tecto.2015.05.003

Komiya, T., Yamamoto, S. *et al.* 2017. A prolonged granitoid formation in Saglek Block, Labrador: zonal growth and crustal reworking of continental crust in the Eoarchean. *Geoscience Frontiers*, **8**, 355–385, https://doi.org/10.1016/j.gsf.2016.06.013

Krogh, T.E. & Kamo, S.L. 2006. Precise U–Pb zircon ID-TIMS ages provide an alternative interpretation to early ion microprobe ages and new insights into Archean crustal processes, northern Labrador. *In*: Reimold, W.U. & Gibson, R.L. (eds) *Processes on the Early Earth*. Geological Society of America, Special Papers, **405**, 91–103, https://doi.org/10.1130/2006.2405(06)

Kusiak, M.A., Dunkley, D.J. *et al.* 2018. Peak to post-peak thermal history of the Saglek Block of Labrador: A multiphase and multi-instrumental approach to geochronology. *Chemical Geology*, **484**, 210–223, https://doi.org/10.1016/j.chemgeo.2017.10.033

Ludwig, K.R. 2001. *User's Manual for Isoplot/Ex v. 3.0: a Geochronological Toolkit for Microsoft Excel*. Berkeley Geochronological Center, Special Publication, **1a**.

Ludwig, K.R. 2009. *Squid 2.50, A User's Manual*. Berkeley Geochronological Center, Special Publication, **5**.

Middlemost, E.A.K. 1994. Naming materials in the magma/igneous rock system. *Earth-Science Reviews*, **37**, 215–224, https://doi.org/10.1016/0012-8252(94)90029-9

Morgan, W.C. 1975. Geology of the Precambrian Ramah Group and basement rocks in the Nachvak Fiord-Saglek Fiord area, north Labrador. *Geological Survey of Canada*, **74**.

Morino, P., Caro, G., Reisbeg L. & Schumacher, A. 2017. Chemical stratification in the post-magma ocean Earth inferred from coupled 146,147Sm–142,143Nd systematics in ultramafic rocks of the Saglek block (3.25–3.9 Ga; northern Labrador, Canada). *Earth and Planetary Science Letters*, **463**, 136–150, https://doi.org/10.1016/j.epsl.2017.01.044

Næraa, T., Kemp, A.I.S., Scherstén, A., Rehnström, E.F., Rosing, M.T. & Whitehouse, M.J. 2014. A lower crustal mafic source for the *ca.* 2550 Ma Qôrqut Granite Complex in southern West Greenland. *Lithos*, **192–195**, 291–304, https://doi.org/10.1016/j.lithos.2014.02.013

Nutman, A.P. & Collerson, K.D. 1991. Very early Archean crustal-accretion complexes preserved in the North Atlantic Craton. *Geology*, **19**, 791–794, https://doi.org/10.1130/0091-7613(1991)019<0791:VEACAC>2.3.CO;2

Nutman, A.P. & Friend, C.R.L. 2007. Adjacent terranes with *ca.* 2715 and 2650 Ma high-pressure metamorphic assemblages in the Nuuk region of the North Atlantic Craton, southern West Greenland: Complexities of Neoarchaean collisional orogeny. *Precambrian Research*, **155**, 159–203, https://doi.org/10.1016/j.precamres.2006.12.009

Nutman, A.P., Friend, C., Barker, S.L.L. & McGregor, V.R. 2004. Inventory and assessment of Palaeoarchaean gneiss terrains and detrital zircons in southern West Greenland. *Precambrian Research*, **135**, 281–314, https://doi.org/10.1016/j.precamres.2004.09.002

Nutman, A.P., Friend, C. & Hiess, J. 2011. Setting of the 2560 Ma Qorqut Granite Complex in the Archean crustal evolution of Southern West Greenland. *American Journal of Science*, **310**, 1081–1114, https://doi.org/10.2475/09.2010.12

Nutman, A.P., Bennett, V.C., Friend, C.R.L., Hidaka, H., Yi, K., Lee, S.R. & Kamiichi, T. 2013. The Itsaq Gneiss Complex of Greenland: Episodic 3900 to 3660 Ma juvenile crust formation and recycling in the 3660 to 3600 Ma Isukasian orogeny. *American Journal of Science*, **313**, 877–911, https://doi.org/10.2475/09.2013.03

O'Connor, J.T. 1965. *A Classification for Quartz-rich Igneous Rocks Based on Feldspar Ratios*. US Geological Survey, Professional Papers, **B525**, 79–84.

Rivers, T., Mengel, F., Scott, D.J., Campbell, L.M. & Goulet, N. 1996. Torngat Orogen – a Palaeoproterozoic example of a narrow doubly vergent collisional orogeny. *In*: Brewer, T.S. (ed.) *Precambrian Crustal Evolution in the North Atlantic Region*. Geological Society, London, Special Publications, **112**, 117–136, https://doi.org/10.1144/GSL.SP.1996.112.01.07

Rosing, M.T., Nutman, A.P. & Lofqvist, L. 2001. A new fragment of the early earth crust: the Aasivik terrane of West Greenland. *Precambrian Research*, **105**, 115–128, https://doi.org/10.1016/S0301-9268(00)00107-8

Ryan, B. & Martineau, Y. 2012. *Revised and coloured edition of 1992 map showing the geology of the Saglek Fjord–Hebron Fjord area, Labrador (NTS 14L/2,3,6,7). Scale: 1:100000 Map 2012–2015*. Government of Newfoundland and Labrador, Department of Natural Resources, Geological Survey, Open File, **2014L/0091**. (Update of map originally released as Newfoundland Department of Mines and Energy, Geological Survey Branch, Map 92-18B and Geological Survey of Canada, Open File 2466.)

Sałacińska, A., Kusiak, M.A., Whitehouse, M.J., Dunkley, D.J., Wilde, S.A. & Kielman, R. 2018. Complexity of the early Archean Uivak Gneiss: Insights from Tigigakyuk Inlet, Saglek Block, Labrador, Canada and possible correlations with south West Greenland. *Precambrian Research*, **315**, 103–119, https://doi.org/10.1016/j.precamres.2018.07.011

Sałacińska, A., Kusiak, M.A., Whitehouse, M.J., Dunkley, D.J., Wilde, S.A., Kielman, R. & Król, P. 2019. Gneiss forming events in the Saglek Block, Labrador: a reappraisal of the Uivak Gneiss. *International Journal of Earth Sciences*, **108**, 753–778, https://doi.org/10.1007/s00531-019-01677-y

Schiøtte, L., Compston, W. & Bridgwater, D. 1989. Ion-probe U–Th–Pb zircon dating of polymetamorphic orthogneisses from northern Labrador, Canada. *Canadian Journal of Earth Sciences*, **26**, 1533–1556, https://doi.org/10.1139/e89-131

Schiøtte, L., Noble, S. & Bridgwater, D. 1990. U–Pb mineral ages from northern Labrador: Possible evidence for interlayering of Early and Middle Archean tectonic slices. *Geoscience Canada*, **17**, 227–231.

Schiøtte, L., Nutman, A.P. & Bridgwater, D. 1992. U–Pb ages of single zircons within Upernavik metasedimentary rocks and regional implications for the tectonic evolution of the Archean Nain Province, Labrador. *Canadian Journal of Earth Sciences*, **29**, 260–276, https://doi.org/10.1139/e92-024

Scott, D.J. 1995. U–Pb geochronology of the Nain craton on the eastern margin of the Torngat Orogen, Labrador. *Canadian Journal of Earth Sciences*, **32**, 1859–1869, https://doi.org/10.1139/e95-143

Shimojo, M., Yamamoto, S. *et al.* 2016. Occurrence and geochronology of the Eoarchean, ~3.9 Ga, Iqaluk Gneiss in the Saglek Block, northern Labrador, Canada: evidence for the oldest supracrustal rocks in the world. *Precambrian Research*, **278**, 218–243, https://doi.org/10.1016/j.precamres.2016.03.018

Stacey, J.S. & Kramers, J.D. 1975. Approximation of terrestrial lead isotope evolution by a two-stage model. *Earth and Planetary Science Letters*, **26**, 207–221, https://doi.org/10.1016/0012-821X(75)90088-6

Stern, R.A. 2001. *A new isotopic and trace-element standard for the ion microprobe: preliminary thermal ionization mass spectrometry (TIMS) U–Pb and electron-microprobe data; Radiogenic Age and Isotopic Studies: Report 14*. Geological Survey Canada, Current Research, **2001-F**.

Stern, R.A., Bodorkos, S., Kamo, S.L., Hickman, A.H. & Corfu, F. 2009. Measurement of SIMS instrumental mass fractionation of Pb isotopes during zircon dating. *Geostandards and Geoanalytical Research*, **33**, 145–168, https://doi.org/10.1111/j.1751-908X.2009.00023.x

St-Onge, M.R., Van Gool, J.A.M., Garde, A.A. & Scott, D.J. 2009. Correlation of Archaean and Palaeoproterozoic units between northeastern Canada and western Greenland: constraining the pre-collisional upper plate accretionary history of the Trans-Hudson orogen. *In*: Cawood, P.A. & Kröner, A. (eds) *Earth Accretionary Systems in Space and Time*. Geological Society, London, Special Publications, **318**, 193–235, https://doi.org/10.1144/SP318.7

Szilas, K., Maher, K. & Bird, D.K. 2016. Aluminous gneiss derived by weathering of basaltic source rocks in the Neoarchean Storø Supracrustal Belt, southern West Greenland. *Chemical Geology*, **441**, 63–80, https://doi.org/10.1016/j.chemgeo.2016.08.013

Szilas, K., Tusch, J., Hoffmann, J.E., Garde, A.A. & Münker, C. 2017. Hafnium isotope constraints on the origin of Mesoarchaean andesites in southern West Greenland, North Atlantic Craton. *In*: Halla, J., Whitehouse, M.J., Ahmad, T. & Bagai, Z. (eds) *Crust–Mantle Interactions and Granitoid Diversification: Insights from Archaean Cratons*. Geological Society, London, Special Publications, **449**, 19–38, https://doi.org/10.1144/SP449.2

Tashiro, T., Ishida, A. *et al.* 2017. Early trace of life from 3.95 Ga sedimentary rocks in Labrador, Canada. *Nature*, **549**, 516–518, https://doi.org/10.1038/nature24019

Taylor, F.C. 1971. A revision of Precambrian structural provinces in northeastern Quebec and northern Labrador. *Canadian Journal of Earth Sciences*, **8**, 579–584, https://doi.org/10.1139/e71-059

Van Kranendonk, M.J. 1996. Tectonic evolution of the Paleoproterozoic Torngat Orogen: Evidence from pressure–temperature–time–deformation paths in the North River map area, Labrador. *Tectonics*, **15**, 843–869, https://doi.org/10.1029/95TC03771

Van Kranendonk, M. & Ermanovics, I.F. 1990. Structural evolution of the Hudsonian Torngat Orogen in the North River map area, Labrador: evidence for east–west transpressive collision of Nain and Rae continental blocks. *Geoscience Canada*, **17**, 283–288.

Van Kranendonk, M. & Helmstaedt, H. 1990. Late Archean geologic history of the Nain Province, North River–Nutak map area, Labrador, and its tectonic significance. *Geoscience Canada*, **17**, 231–237.

Wanless, R.K., Stevens, R.D., Lachance, G.R. & Delabio, R.N. 1970. K–Ar isotopic ages Report 9; Age determinations and geological studies. *Geological Survey of Canada Paper*, **69**, 1–78.

Wanless, R.K., Stevens, R.D., Lachance, G.R. & Delabio, R.N. 1974. Isotopic ages Report 12; Age determinations and geological studies. *Geological Survey Canada Paper*, **74**, 60–63.

Wasteneys, H.A., Wardle, R.J. & Krogh, T.E. 1996. Extrapolation of tectonic boundaries across the Labrador shelf: U–Pb geochronology of well samples. *Canadian Journal of Earth Sciences*, **33**, 1308–1324, https://doi.org/10.1139/e96-099

Watson, E.B., Wark, D.A. & Thomas, J.B. 2006. Crystallization thermometers for zircon and rutile. *Contributions to Mineralogy and Petrology*, **151**, 314–433, https://doi.org/10.1007/s00410-006-0068-5

Wendt, J.I. & Collerson, K.D. 1999. Early Archean U/Pb fractionation and timing of late Archean high-grade metamorphism in the Saglek–Hebron segment of the North Atlantic Craton. *Precambrian Research*, **93**, 281–297, https://doi.org/10.1016/S0301-9268(98)00093-X

Whitehouse, M.J. & Kamber, B.S. 2005. Assigning dates to thin gneissic veins in high-grade metamorphic terranes: A cautionary tale from Akilia, southwest Greenland. *Journal of Petrology*, **46**, 291–318, https://doi.org/10.1093/petrology/egh075

Whitehouse, M.J., Dunkley, D.J., Kusiak, M.A. & Wilde, S.A. 2019. On the true antiquity of Eoarchean chemofossils – assessing the claim for Earth's oldest biogenic graphite in the Saglek Block of Labrador. *Precambrian Research*, **323**, 70–81, https://doi.org/10.1016/j.precamres.2019.01.001

Wiedenbeck, M., Allé, P. *et al.* 1995. Three natural zircon standards for U–Th–Pb, Lu–Hf, trace-element and REE analyses. *Geostandards Newsletter*, **19**, 1–23, https://doi.org/10.1111/j.1751-908X.1995.tb00147.x

Zeck, H.P. & Whitehouse, M.J. 1999. Hercynian, Pan-African, Proterozoic and Archean ion-microprobe zircon ages for a Betic–Rif core complex, Alpine belt, W Mediterranean – consequences for its *P–T–t* path. *Contributions to Mineralogy and Petrology*, **134**, 134–149, https://doi.org/10.1007/s004100050474